




Article

# Cu-Mg-Fe-O-(Ce) Complex Oxides as Catalysts of Selective Catalytic Oxidation of Ammonia to Dinitrogen (NH<sub>3</sub>-SCO)

Sylwia Górecka<sup>1,\*</sup> , Kateřina Pacultová<sup>1</sup> , Kamil Górecki<sup>1</sup>, Aneta Smýkalová<sup>1,2</sup>, Katarzyna Pamin<sup>3</sup> and Lucie Obalová<sup>1</sup> 

<sup>1</sup> Institute of Environmental Technology, VŠB – Technical University of Ostrava, 17. listopadu 15/2172, 708 00 Ostrava, Czech Republic; katerina.pacultova@vsb.cz (K.P.); kamil.maciej.gorecki@vsb.cz (K.G.); aneta.smykalova@vsb.cz (A.S.); lucie.obalova@vsb.cz (L.O.)

<sup>2</sup> Faculty of Materials Science and Technology, Department of Chemistry, VŠB-Technical University of Ostrava, 17. listopadu 15/2172, 708 00 Ostrava, Czech Republic

<sup>3</sup> Jerzy Haber Institute of Catalysis and Surface Chemistry Polish Academy of Sciences, Niezapominajek 8, 30-239 Kraków, Poland; ncpamin@cyf-kr.edu.pl

\* Correspondence: sylwia.gorecka@vsb.cz; Tel.: +420-597-327-315

Received: 30 November 2019; Accepted: 26 January 2020; Published: 28 January 2020



**Abstract:** Multicomponent oxide systems 800-Cu-Mg-Fe-O and 800-Cu-Mg-Fe-O-Ce were tested as catalysts of selective catalytic oxidation of ammonia to dinitrogen (NH<sub>3</sub>-SCO) process. Materials were obtained by calcination of hydrotalcite-like compounds at temperature 800 °C. Some catalysts were doped with cerium by the wet impregnation method. Not only simple oxides, but also complex spinel-like phases were formed during calcination. The influence of chemical composition, especially the occurrence of spinel phases, copper loading and impregnation by cerium, were investigated. Materials were characterized by several techniques: X-ray diffraction (XRD), Fourier-transform infrared spectroscopy (FT-IR), low-temperature nitrogen adsorption (BET), cyclic voltammetry (CV), temperature programmed reduction (H<sub>2</sub>-TPR), UV-vis diffuse reflectance spectroscopy and scanning electron microscopy (SEM). Examined oxides were found to be active as catalysts of selective catalytic oxidation of ammonia with high selectivity to N<sub>2</sub> at temperatures above 300 °C. Catalysts with low copper amounts (up to 12 wt %) impregnated by Ce were slightly more active at lower temperatures (up to 350 °C) than non-impregnated samples. However, when an optimal amount of copper (12 wt %) was used, the presence of cerium did not affect catalytic properties. Copper overloading caused a rearrangement of present phases accompanied by the steep changes in reducibility, specific surface area, direct band gap, crystallinity, dispersion of CuO active phase and Cu<sup>2+</sup> accessibility leading to the decrease in catalytic activity.

**Keywords:** selective catalytic oxidation; ammonia; NH<sub>3</sub>-SCO; mixed metal oxides; MgFe<sub>2</sub>O<sub>4</sub> type spinel oxides; Cu-Fe-Ce based oxides; Cu-Ce redox couples; Cu-Fe redox couples

## 1. Introduction

Ammonia, besides nitrogen and sulfur oxides, non-methane volatile organic compounds and fine particulate matter (PM<sub>2.5</sub>), belongs to the group of air pollutants whose emissions are strictly monitored, and for which long-term emission reduction programs were introduced (e.g., National Emission Ceilings Directive 2001/81/EC (NECD) and Gothenburg Protocol). On the basis of the most recent data, ammonia emissions have been estimated at about 5 600 kt y<sup>-1</sup> [1]. The main sources of emissions include agriculture (comprises 94% of total emissions [2]), industry (including energy production and use), road transport and waste [2–5]. Environmental reports show that total emissions of ammonia, thanks

to the implementation of stricter regulations, decrease each year [6]. However, there are sectors where ammonia emissions increased drastically in recent years, and a further increase is expected. These are transportation and stationary sources equipped with selective catalytic reduction (SCR)  $\text{NO}_x/\text{NH}_3$  or non-selective catalytic reduction (NSCR) units. The reason is stricter regulation of  $\text{NO}_x$  emissions, which are often achieved by over stoichiometric dosage of ammonia resulting in ammonia slip. In the transportation sector, besides ammonia slip from SCR  $\text{NO}_x/\text{NH}_3$  processes, the formation of ammonia as a byproduct of three way catalysts was also observed [7,8]. Because of the significant toxicity of  $\text{NH}_3$ , efficient removal methods of ammonia should be studied. One of the most promising methods of ammonia emission control is selective catalytic oxidation of ammonia to dinitrogen ( $\text{NH}_3\text{-SCO}$ ) [9,10]. The application areas for  $\text{NH}_3\text{-SCO}$  include transportation, treatment of waste gases from biomass gasification, chemical production processes and ammonia slip from SCR  $\text{NO}_x/\text{NH}_3$  processes. Ammonia slip could be observed in the case of fuel combustion, refining of mineral oils and gases, production of cement, lime and magnesium oxides, manufacturing of glass and production of pulp, paper and boards [2,3,5,9–11].

Selective catalytic oxidation of ammonia to dinitrogen is a complex process that includes a series of reactions (main, side and follow-up) that may lead to the formation of different products. The mechanism of the  $\text{NH}_3\text{-SCO}$  reaction is dependent on catalyst type and process conditions. However, in most cases, the first step is related to ammonia adsorption at active centers of the material surface. In general, selective catalytic oxidation of ammonia; could occur via three different ways (i) imide mechanism [9,12]; (ii) hydrazine mechanism [13–15] and (iii) internal selective catalytic reduction (i-SCR) [13,16,17]. The first mechanism, also known as the Zawadzki mechanism, was proposed for Pt and Ru based catalysts. In the first stage, adsorbed ammonia is oxidized to imide (NH) which reacts with dissociated oxygen to nitrosyl (HNO). The main reaction that leads to the formation of  $\text{N}_2$  and  $\text{H}_2\text{O}$  occurs between imide and nitrosyl [9,12]. The hydrazine mechanism was proposed for transition metal-based catalysts and processes performed under limited  $\text{O}_2$  concentration. The mechanism assumes the formation of amides ( $\text{NH}_2$ ) via oxidation of absorbed ammonia by molecular oxygen, and their surface recombination that leads to the formation of hydrazine-like products  $\text{NH}_2\text{-NH}_2$ . Intermediate species are oxidized during the next step to dinitrogen [9]. The last mechanism is most probable for oxide-based catalysts. According to i-SCR, part of adsorbed ammonia is oxidized by molecular oxygen to nitric oxide, which is in the next step oxidized by ammonia to dinitrogen [9]. The reaction rate of  $\text{NH}_3\text{-SCO}$  process is limited by several issues, such as: Dissociation of molecular oxygen and recombination of  $\text{OH}^-$  surface groups (i); the desorption of products from the material surface (ii and iii). All of the mentioned mechanisms are characterized by the occurrence of side reactions that lead to the formation of nitric oxide (NO), nitrous oxide ( $\text{N}_2\text{O}$ ) and/or nitrogen dioxide ( $\text{NO}_2$ ). The desired product of the  $\text{NH}_3\text{-SCO}$  reaction is dinitrogen, and selectivity, thus, represents an important catalyst characteristic. Selectivity to  $\text{N}_2$  depends on the catalyst type, its phase and chemical composition, as well as physicochemical properties like specific surface area or reducibility.

Copper-based materials were found to be effective catalysts of the  $\text{NH}_3\text{-SCO}$  reaction with high selectivity to dinitrogen. Jabłońska et al. [10] summarized the relationship between the catalysts' composition and their efficiency. Cu-Mg-Al-O hydrotalcite derived mixed metal oxides represent a group of highly efficient materials of  $\text{NH}_3\text{-SCO}$ . This group is characterized by homogeneously dispersed active centers, thermal stability and a relatively high surface area. Copper loading at about 5–8 wt % allows reaching 100% ammonia conversion at temperatures below 500 °C with  $\text{N}_2$  selectivity of about 86–90%. An increase of the copper loading allows shifting the conversion temperature to lower range (even 100–150 °C lower), however, the selectivity to dinitrogen drops significantly. Literature results show that the presence of highly dispersed and easily reducible CuO species could increase the selectivity to  $\text{N}_2$  [18]. A similar effect has been reported for Ce-Cu-oxides [17,19,20]. In the case of cerium doped oxides, an increase of catalytic activity was related to the activation of lattice oxygen, which is a result of Cu-Ce redox couple occurrence at the surface.

The presented study is focused on the characterization of Cu-Mg-Fe-Ce based materials and their efficiency as catalysts of selective catalytic oxidation of ammonia. These catalysts have been obtained by calcination of hydrotalcite-like materials at 800 °C. The relatively high temperature of calcination causes the formation of spinel structures next to simple oxide systems. Previously reported Cu-based materials active as catalysts of NH<sub>3</sub>-SCO process were characterized by simple CuO structure deposited at the precursor surface (e.g., CuO/Al<sub>2</sub>O<sub>3</sub>), and calcined at lower temperatures, approximately 500–600 °C [21]. Materials obtained at higher temperatures have been reported as inactive or were characterized by sufficient conversion only at high temperatures. As mentioned previously, the Cu amount above 10 wt % results in increasing of the NH<sub>3</sub> removal efficiency and decreasing of selectivity to dinitrogen with a simultaneous increase of selectivity to NO. Our aim was to obtain catalysts active at low-temperature range (up to 350 °C). Chemical composition of the samples was selected to determine the effect of Cu, Fe and Ce loading on NH<sub>3</sub>-SCO, while high calcination temperature was chosen to study the influence of spinel phase formation on catalytic activity and selectivity to dinitrogen. According to the literature [18,22–25], iron and cerium-based materials show high efficiency in low-temperature catalytic reduction of NO to N<sub>2</sub>. Therefore, the addition of Fe and Ce should result in increasing the N<sub>2</sub> selectivity in NH<sub>3</sub>-SCO processes occurring over Cu-rich catalysts.

Our research shows that the proposed oxide systems are active as catalysts of selective catalytic oxidation of ammonia; however, neither Ce modified, or unmodified catalysts reached 100% of ammonia conversion. The highest removal efficiency (about 70%) was observed for samples with the optimal copper amount, while overloading with copper resulted in a significant decrease in removal efficiency (below 20%).

## 2. Results and Discussion

The experimental results of the characterization of two series of Cu-Mg-Fe-O mixed metal oxides obtained by calcination of hydrotalcite-like materials are described. The prepared mixed metal oxides were tested as catalysts of low-temperature selective catalytic oxidation of ammonia to dinitrogen. The results of ammonia removal efficiency and N<sub>2</sub> selectivity for two oxide series, 800-Cu-Mg-Fe-O and 800-Cu-Mg-Fe-O-Ce, are presented and discussed.

### 2.1. Characterisation of Hydrotalcite-Like Materials

Chemical composition of the obtained hydrotalcite-like materials was determined by X-ray fluorescence spectroscopy (Table 1). The intended and actual Cu:Fe molar ratios were calculated. The actual values of Cu:Fe ratio are close to those used for precipitation.

**Table 1.** Physico-chemical properties of Cu-Mg-Fe hydrotalcite precursors.

Sample	Cu/Mg/Fe Intended Chemical Composition, % *	Intended Molar Cu:Fe Ratio, -	XRF Chemical Composition, wt %			Actual Molar Cu:Fe Ratio, -	Cell Parameters, nm	
			Cu	Mg	Fe		a	c
HT-Mg-Fe	0/67/33	-	0	14.6	23.4	-	0.311	2.361
HT-Cu5-Mg-Fe	5/62/33	0.15	3.1	10.3	18.7	0.16	0.311	2.358
HT-Cu7-Mg-Fe	7/60/33	0.21	4.7	11	20.2	0.23	0.311	2.354
HT-Cu10-Mg-Fe	10/57/33	0.30	5.9	8.6	18.8	0.32	0.305	2.298
HT-Cu12-Mg-Fe	12/55/33	0.36	7.3	8.6	18.6	0.39	0.311	2.343
HT-Cu15-Mg-Fe	15/52/33	0.45	8.0	7.3	16.6	0.48	0.312	2.343

\*% mol. of total metals amount.

Phase composition analysis and infrared spectroscopy measurements of as-synthesized hydrotalcite-like materials (Figure S1, Supplementary) exhibit hydrotalcite structure (hexagonal lattice with rhombohedral R3m space group symmetry) [26–28]. Characteristic XRD patterns (Figure S1a, Supplementary) ascribed to network plane (003), (006), (012), (015), (018), (110) and (113) were observed at positions—13, 27, 39, 25, 54, 70 and 71 °2θ, respectively. Calculated cell parameters (a and c) are typical for pyroaurite [29].

The results of infrared spectroscopy measurements (Figure S1b, Supplementary) prove the occurrence of species characteristic for hydrotalcite-like materials: Interlayer carbonate anions, structural water or M-OH bond where M is the corresponding metal group [30–32].

## 2.2. Properties of the Mixed Metal Oxides

The codes and intended chemical composition of the calcined samples are given in Table 2.

**Table 2.** Codes of calcined samples and intended (int.) chemical composition.

Series 800-Cu-Mg-Fe-O				Series 800-Cu-Mg-Fe-O-Ce				
Sample Code	Int. Chemical Composition, mol % *			Sample Code	Int. Chemical Composition, mol % *			
	Cu	Mg	Fe		Cu	Mg	Fe	Ce
800-Mg-Fe	0	67	33	800-Mg-Fe-Ce	0	65.3	32.2	2.5
800-Cu5-Mg-Fe	5	62	33	800-Cu5-Mg-Fe-Ce	4.9	60.5	32.2	2.5
800-Cu7-Mg-Fe	7	60	33	800-Cu7-Mg-Fe-Ce	6.8	58.5	32.2	2.5
800-Cu10-Mg-Fe	10	57	33	800-Cu10-Mg-Fe-Ce	9.7	55.7	32.2	2.5
800-Cu12-Mg-Fe	12	55	33	800-Cu12-Mg-Fe-Ce	11.7	53.6	32.2	2.5
800-Cu15-Mg-Fe	15	52	33	800-Cu15-Mg-Fe-Ce	14.6	50.7	32.2	2.5

\*% mol. of total metals amount.

### 2.2.1. Chemical Composition

The results of chemical analysis of 800-Cu-Mg-Fe-O and 800-Cu-Mg-Fe-O-Ce catalysts are summarized in Tables 3 and 4, respectively. The comparison of calculated and intended Cu:Fe molar ratios shows that the intended chemical composition is in accordance with the measured results.

**Table 3.** Chemical composition of the 800-Cu-Mg-Fe-O catalysts.

Sample	Wt. %			Cu:Fe Molar Ratio	Cu:Fe Molar Ratio
	Cu	Mg	Fe	Calc. *	Int. **
800-Mg-Fe		21.0	33.8		
800-Cu5-Mg-Fe	5.2	17.0	31.8	0.14	0.15
800-Cu7-Mg-Fe	7.4	12.3	28.9	0.22	0.21
800-Cu10-Mg-Fe	10.0	14.5	30.8	0.29	0.30
800-Cu12-Mg-Fe	12.0	10.6	28.5	0.37	0.36
800-Cu15-Mg-Fe	13.6	9.9	25.6	0.46	0.45

\* calculated molar ratio \*\* intended molar ratio.

**Table 4.** Chemical composition of the 800-Cu-Mg-Fe-O-Ce.

Sample	Wt %				Cu:Fe Molar Ratio		Cu:Ce Molar Ratio	
	Cu	Mg	Fe	Ce	Int. **	Calc. *	Int. **	Calc. *
800-Mg-Fe-Ce		20.6	31.0	4.2				
800-Cu5-Mg-Fe-Ce	4.6	13.4	28.3	4.3	0.15	0.14	2.0	2.35
800-Cu7-Mg-Fe-Ce	6.7	14.7	29.6	4.4	0.21	0.19	2.8	3.35
800-Cu10-Mg-Fe-Ce	9.3	10.9	28.6	4.8	0.30	0.28	4.0	4.27
800-Cu12-Mg-Fe-Ce	10.9	12.4	28.7	4.0	0.36	0.33	4.8	6.0
800-Cu15-Mg-Fe-Ce	11.9	10.2	24.8	4.0	0.45	0.42	6.0	6.6

\* calculated molar ratio \*\* intended molar ratio.

### 2.2.2. Phase Composition and Morphology

Powder XRD patterns of the calcined samples are presented in Figure 1. The obtained mixed metal oxides exhibited various oxide structures that depended on the copper amount. Characteristic diffraction lines occurring at approximately 21, 35, 41, 43, 50, 63, 67, 74, 78, 85 and 88 °2θ were ascribed to spinel-like phases labelled as: (Cu,Mg)Fe<sub>2</sub>O<sub>3</sub> (ICDD PDF-2 card No 01-076-9731). As expected [14,18,33], high temperature of calcination (800 °C) favors the formation of complex oxide structures; therefore,

these patterns were observed for each sample irrespective of the copper loading. Apart from the complex spinel phases, characteristic diffraction lines for simple oxides like periclase (MgO) and tenorite (CuO) were also found. The periclase lines occurred at positions 42, 50, 73 and 90 °2 $\theta$  (ICCD PDF-2 card No 01-071-1176), while tenorite lines occurred at positions—38, 41, 45, 57, 63, 69, 73, 79, 81 and 87 °2 $\theta$  (ICCD PDF-2 card No 01-080-1917). While periclase presence was detectable by XRD in all samples, the lines characteristic for CuO phases could be observed only for samples with higher copper loading (800-Cu10-Mg-Fe, 800-Cu10-Mg-Fe-Ce, 800-Cu12-Mg-Fe, 800-Cu12-Mg-Fe-Ce, 800-Cu15-Mg-Fe and 800-Cu-15-Fe-Ce). It could be assumed that the formation of tenorite depends on the copper content. In the case of samples with lower Cu loading (800-Cu5-Mg-Fe, 800-Cu5-Mg-Fe-Ce, 800-Cu7-Mg-Fe and 800-Cu7-Mg-Fe-Ce), copper cations could be built into spinel-like or periclase structure. Copper cations could also form amorphous structures or small CuO primary particles well dispersed on the surface and not detectable by XRD. Substitution of some magnesium cations (that build spinel and periclase oxides) by Cu is possible, due to the similar ionic radii of Cu (0.057 nm) and Mg (0.057 nm) in tetrahedral coordination [34]. The obtained results suggest that the formation of a well-developed spinel phase is more favorable than the formation of CuO. It could be explained by calcination temperature, which highly influences the thermal transformation of hydrotalcite-like materials, as well as the properties of calcination products. At lower temperatures (below 600 °C), these structures are characterized by low-crystalline simple oxides or even by semi-amorphous structures that could be easily reversed to layered hydrotalcite form when exposed to moisture [32,35–38]. Higher temperatures of calcination promote the formation of more thermally stable species and reorganization of the already existing structures into more complex ones.

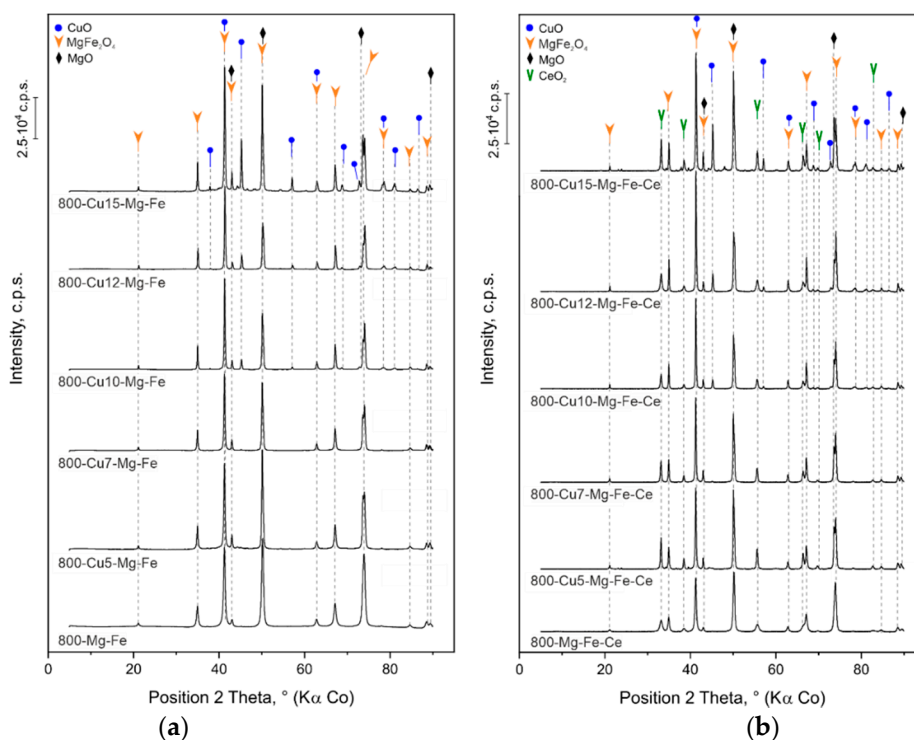


**Figure 1.** Phase composition of mixed metal oxides (a) 800-Cu-Mg-Fe-O and (b) 800-Cu-Mg-Fe-O-Ce.

Diffuse reflectance spectroscopy (UV-vis-DRS) and further analysis of optical characteristics with the use of Tauc's plot gives estimates for direct optical band gaps ( $E_g^d$ ) of spinel-like  $MgFe_2O_4$  structures (Table 5). Stoichiometric  $MgFe_2O_4$  is characterized by a direct band gap at about  $E_g^d = 2.0\text{--}2.7$  eV, while  $CuFe_2O_4$  species are characterized by a smaller direct band gap at about  $E_g^d = 1.9\text{--}2.0$  eV [39–42]. The values estimated for samples 800-Cu5-Mg-Fe, 800-Cu5-Mg-Fe-Ce, 800-Cu7-Mg-Fe and 800-Cu7-Mg-Fe-Ce are close to 2.4–2.47 eV, which corresponds to the reference

samples 800-Mg-Fe and 800-Mg-Fe-Ce. With the increasing amount of copper, the estimated values of  $E_g^d$  decrease to about 2.10–2.20 eV. The obtained results allow us to conclude that in the case of samples with a higher copper amount, part of the magnesium in  $MgFe_2O_4$  is substituted by Cu, which results in the formation of non-stoichiometric  $Cu_xMg_{1-x}Fe_2O_4$  spinels with high Cu amount. It was not possible to distinguish these spinel forms by XRD, because the characteristic diffraction lines of both structures could be found at similar positions. Band gap estimation shows that the addition of Ce does not influence the direct band gap of the obtained catalysts.

**Table 5.** Direct band gap energy (eV), crystallite sizes (nm) and XRD intensity ratios for Cu-Mg-Fe-O and Cu-Mg-Fe-O-Ce mixed metal oxides.

Sample	Direct Band Gap Energy, eV	I(440)/I(222) *	Crystallite Size **, nm			
			CuO	MgO	MgFe <sub>2</sub> O <sub>4</sub>	CeO <sub>2</sub>
800-Mg-Mg-Fe	2.46	-	-	16	19	-
800-Cu5-Mg-Fe	2.44	1.13	-	36	28	-
800-Cu7-Mg-Fe	2.44	1.27	-	41	31	-
800-Cu10-Mg-Fe	2.10	1.54	21	38	37	-
800-Cu12-Mg-Fe	2.09	1.72	34	40	30	-
800-Cu15-Mg-Fe	2.15	0.93	35	41	37	-
800-Mg-Fe-Ce	2.47	-	-	22	23	13
800-Cu5-Mg-Fe-Ce	2.46	1.22	-	28	26	20
800-Cu7-Mg-Fe-Ce	2.46	1.36	-	24	26	24
800-Cu10-Mg-Fe-Ce	2.20	1.58	25	43	33	21
800-Cu12-Mg-Fe-Ce	2.12	1.85	30	40	28	16
800-Cu15-Mg-Fe-Ce	2.21	0.98	35	34	26	21

\* Intensity ratio of (440)/(220) diffractions ascribed to Spinel (74 °2θ)/Periclase (73 °2θ) phase. \*\* Determined from XRD.

In the case of samples modified by Ce (800-Cu-Mg-Fe-O-Ce), the XRD patterns exhibit additional characteristic diffraction lines at positions 33, 38, 45, 55, 66, 70 and 82 °2θ related to CeO<sub>2</sub> phase (ICDD PDF-2 card No 01-080-5548). The lines characteristic for individual oxide species are at the same positions irrespective of the copper amount or Ce intercalation, which means that all samples are characterized by a similar cell parameter of individual phases  $a = 0.84$  nm for  $MgFe_2O_4$ ,  $a = 0.42$  nm for MgO,  $a = 0.47$  nm,  $b = 0.34$  nm,  $c = 0.51$  nm for CuO and  $a = 0.51$  nm for CeO<sub>2</sub> oxide. The calculated values correspond well with literature data [29]. The changes in the amount of spinel and periclase phases, due to Cu substitution can be observed from the intensity ratios of individual diffractions of both phases (Table 5). With increasing copper ratio up to 12 mol. %, the spinel amount was increasing in relation to periclase. The opposite trend occurred for further copper amount increase—the spinel/periclase intensity ratio for Cu15-Mg-Fe and Cu15-Mg-Fe-Ce samples was the lowest of all samples. The observed trend confirmed a continuous diminution of periclase phase with increasing copper content.

The crystallite size of each phase was calculated on the basis of characteristic diffraction lines with the use of Debye-Scherrer equation and are summarized in Table 5. The crystallite size of CuO particles (calculated on the basis of line 45 and 57 °2θ) is about 20–35 nm for both series of catalysts. The smallest CuO particles, 21 and 25 nm, were determined for samples 800-Cu10-Mg-Fe and 800-Cu10-Mg-Fe-Ce, respectively. In samples with lower copper loading, the CuO phase was not detected. The crystallite size of CuO increased to 35 nm with the increase of copper loading. The crystallite size of MgO phase (calculated on the basis of line 50, 73 and 43 °2θ) is about 36–41 nm for 800-Cu-Mg-Fe-O samples and 24–43 nm for 800-Cu-Mg-Fe-O-Ce. In the case of materials impregnated by Ce, catalysts 800-Cu5-Mg-Fe-Ce and 800-Cu7-Mg-Fe-Ce were characterized by the smallest crystallite size of 28 and 24 nm, respectively. For both series, reference samples (without Cu) were characterized by the lowest values of 16 nm and 22 nm for 800-Mg-Fe and 800-Mg-Fe-Ce, respectively. The crystallite size

of spinel-like phase (calculated on the basis of line 41, 35, 74 and 67 °2 $\theta$ ) was similar for both series of materials—28–37 nm for 800-Cu-Fe-Mg-O and 26–33 nm for 800-Cu-Fe-Mg-O-Ce. Similar to MgO, also in the case of the spinel phase, reference samples were characterized by the lowest values—19 nm and 23 nm for 800-Mg-Fe and 800-Mg-Fe-Ce, respectively. Crystallite size of CeO<sub>2</sub> (calculated on the basis of line 33, 55 and 66 °2 $\theta$ ) was ranging from 13–24 nm; the lowest value was found out for the reference sample without Cu. Based on the presented results, it could be assumed that Ce addition does not influence the crystallite size of individual phases. However, as expected, copper amount affects the formation of CuO species and influences the spinel crystallite size, probably by incorporation of Cu into the MgFe<sub>2</sub>O<sub>4</sub> phase.

Textural properties were studied by N<sub>2</sub> low-temperature sorption measurements (Table 6). All samples are characterized by a small surface area ranging from 6 to 32 m<sup>2</sup>g<sup>-1</sup> (BET model) for 800-Cu-Mg-Fe-O and from 6 to 27 m<sup>2</sup>g<sup>-1</sup> for 800-Cu-Mg-Fe-O-Ce with a low amount of micropores. The increasing amount of copper in the samples causes a decrease in surface area with a substantial step increase for 800-Cu15-Mg-Fe and 800-Cu15-Mg-Fe-Ce samples. The observed trend can be explained as follows: The reference sample contains a high amount of periclase, with S<sub>BET</sub> surface area of 27–60 m<sup>2</sup>/g [43], and a spinel phase with low crystallinity. The addition of copper causes a decrease in MgO amount, as well as an increase of spinel phase crystallinity. Both factors resulted in the surface area decrease. The step increase of the surface area of 800-Cu15-Mg-Fe and 800-Cu15-Mg-Fe-Ce is related to the presence of the higher amount of CuO phase having S<sub>BET</sub> surface area of about 20–50 m<sup>2</sup>/g [25,44].

**Table 6.** N<sub>2</sub> physisorption results of 800-Cu-Mg-Fe-O and 800-Cu-Mg-Fe-O-Ce mixed oxides.

Sample	BET Surface Area, m <sup>2</sup> g <sup>-1</sup>	t-Plot Micropore Area, m <sup>2</sup> g <sup>-1</sup>	t-Plot External Surface Area, m <sup>2</sup> g <sup>-1</sup>
800-Mg-Fe	32.4	4.0	28.4
800-Cu5-Mg-Fe	14.1	1.3	12.8
800-Cu7-Mg-Fe	8.9	1.6	7.3
800-Cu10-Mg-Fe	6.3	0.5	5.8
800-Cu12-Mg-Fe	6.2	0.5	5.7
800-Cu15-Mg-Fe	18.6	1.4	18.5
800-Mg-Fe-Ce	26.8	4.4	22.4
800-Cu5-Mg-Fe-Ce	17.5	0.1	17.4
800-Cu7-Mg-Fe-Ce	7.6	1.0	6.6
800-Cu10-Mg-Fe-Ce	5.8	0.5	5.4
800-Cu12-Mg-Fe-Ce	6.4	1.2	5.2
800-Cu15-Mg-Fe-Ce	15.3	2.4	12.8

The morphology of chosen calcined samples was examined by scanning electron microscopy (SEM). Micrographs of 800-Cu5-Mg-Fe, 800-Cu10-Mg-Fe and 800-Cu15-Mg-Fe are shown in Figure 2, while micrographs of 800-Cu5-Mg-Fe-Ce, 800-Cu10-Mg-Fe and 800-Cu15-Mg-Fe are shown in Figure 3. The presented images allow observing the specific morphology of catalysts and compare them with the previously discussed results. In general, the morphology of the examined samples is similar to each other, which is connected with comparable crystallite sizes of individual phases and specific surface area. In general, the presented SEM images show shapes typical for magnesioferite (MgFe<sub>2</sub>O<sub>4</sub>) spinel-type structures [40]. In detail, it is possible to observe spherical particles that could be assigned to MgO, CeO<sub>2</sub> and CuO nanoparticles [45,46].

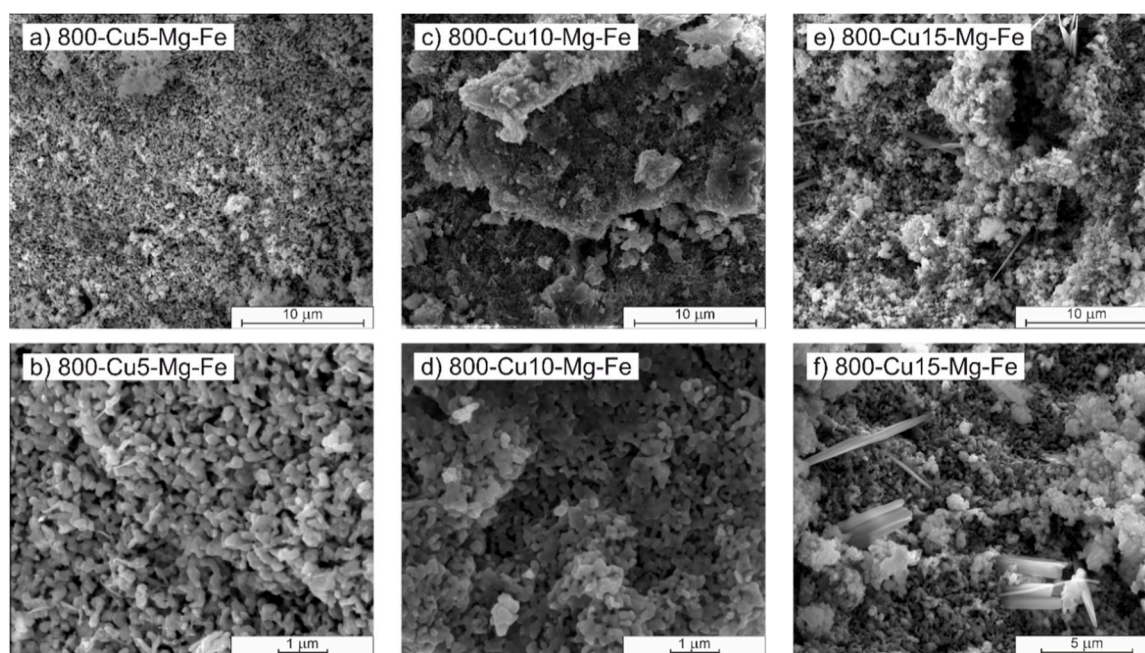


**Figure 2.** SEM micrographs of (a), (b) 800-Cu5-Mg-Fe (BSE mode), (c), (d) 800-Cu10-Mg-Fe (SE mode), (e), (f) 800-Cu15-Mg-Fe (SE mode).

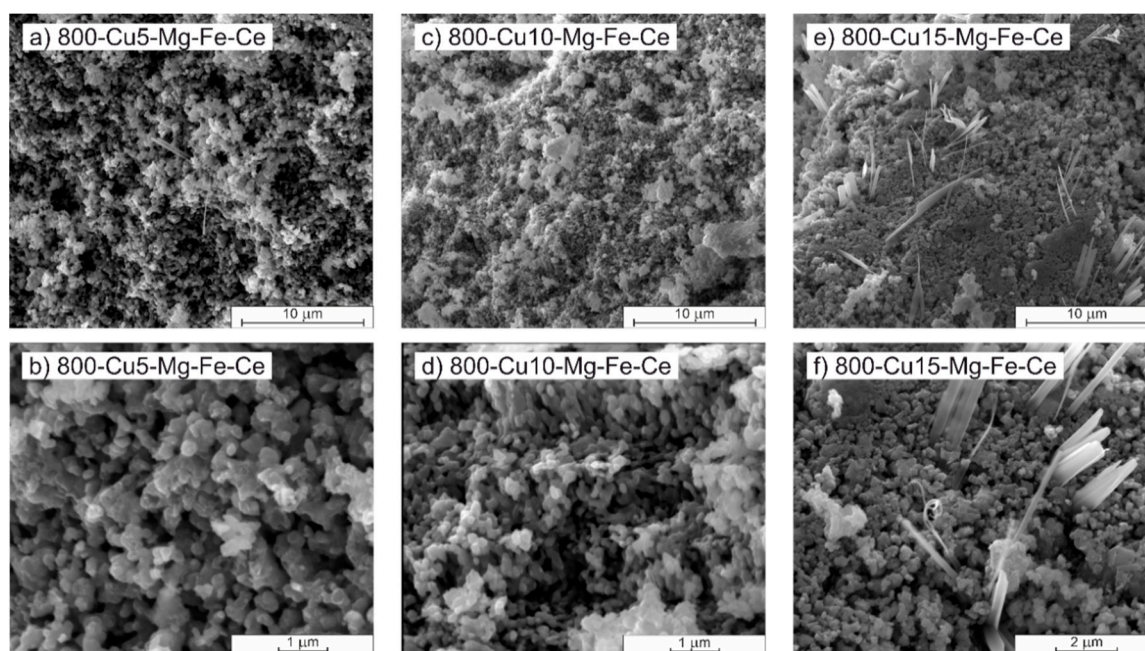


**Figure 3.** SEM micrographs of (a), (b) 800-Cu5-Mg-Fe-Ce (SE mode), (c), (d) 800-Cu10-Mg-Fe-Ce (SE mode), (e), (f) 800-Cu15-Mg-Fe-Ce (SE mode).

The elongated shapes observed in micrographs of 800-Cu15-Mg-Fe (Figure 2e,f) and 800-Cu15-Mg-Fe-Ce (Figure 3e,f) represent a morphology which is characteristic for  $\text{CuFe}_2\text{O}_4$  nanorods [47]. A comparison of the obtained images with band gap estimations and XRD measurements confirms the theory that in the case of samples with a higher copper amount, Cu cations enriched  $\text{MgFe}_2\text{O}_4$  structure and formed non-stoichiometric  $\text{Cu}_x\text{Mg}_{1-x}\text{Fe}_2\text{O}_4$  phases. Estimated values of nanorod diameters determined on the basis of image analysis reveal that  $\text{CuFe}_2\text{O}_4$ -type rods, in the case of 800-Cu15-Mg-Fe catalysts, are characterized by larger diameter (about  $0.63 \mu\text{m}$ ) than 800-Cu15-Mg-Fe-Ce (about  $0.36 \mu\text{m}$ ).



### 2.2.3. Reducibility and Redox Properties

The reducibility of 800-Cu-Mg-Fe-O and 800-Cu-Mg-Fe-O-Ce catalysts was determined by temperature-programmed reduction ( $H_2$ -TPR). The results of the measurements are presented in Figure 4; Figure 5 and Table 7. The low-temperature reduction peaks at 180–250 °C (for 800-Cu-Mg-Fe-O) and 195–260 °C (for 800-Cu-Mg-Fe-O-Ce) were assigned to reduction of well-dispersed copper species in CuO. In the case of the 800-Cu5-Mg-Fe and 800-Cu7-Mg-Fe-Ce samples, the reduction peak in low-temperature range could be related to the formation of small or amorphous CuO species, which were not detected by XRD measurements, but could occur on the material surface. For most samples, except 800-Cu5-Mg-Fe-Ce, the registered reduction peak represents one-step copper reduction  $CuO \rightarrow Cu$ . In the case of samples with the highest Cu content (800-Cu15-Mg-Fe and 800-Cu15-Mg-Fe-Ce), the low temperature peak splitting could be explained by the presence of Cu species with different dispersion levels [15]. Bulk Cu-reach species were also observed in the microphotographs (Figures 2 and 3). On the other hand, the exact ascription of the two-split low-temperature peaks to highly dispersed and non-dispersed (bulk) species is not possible, and we suppose that in the low-temperature peak, the reduction of two different CuO species which differs in the level of dispersion (e.g., small 2D and 3D clusters) takes place. Because  $H_2$  reduction in the bulk process, the same amount of species, but with different dispersion should consume the same amount of hydrogen. However, based on the literature results, it is supposed that different dispersion of CuO species, achieved by different copper amount, strongly influences Cu surface area [48], in other words, the area which is responsible for the catalytic reaction.

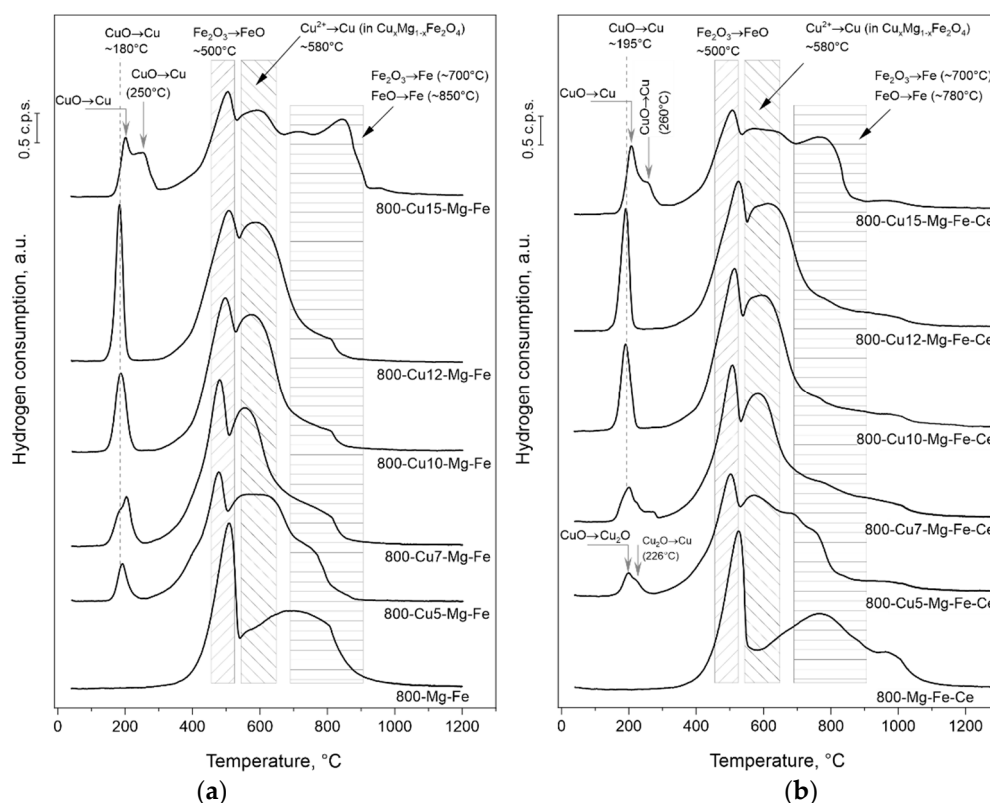


**Figure 4.**  $H_2$ -TPR profiles of obtained catalysts (a) Cu-Mg-Fe-O and (b) Cu-Mg-Fe-O-Ce.

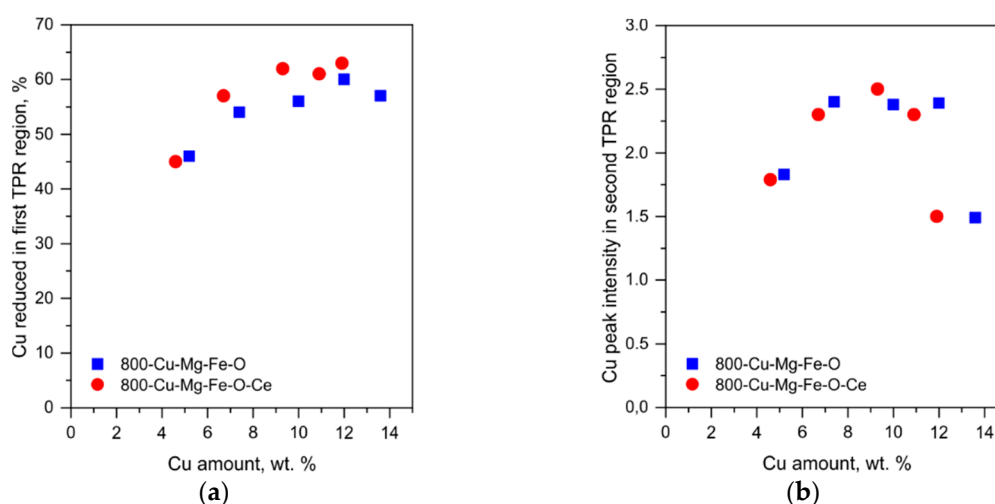


**Figure 5.** Results of H<sub>2</sub>-TPR measurements (a) Cu reduced in first TPR region, (b) Cu peak intensity in the second TPR region.

**Table 7.** TPR-H<sub>2</sub> results.

Sample	H <sub>2</sub> Consumption (50–250 °C), mmol/g	H <sub>2</sub> Consumption (50–900 °C), mmol/g	Cu Reduced at 50–250 °C Region, % *
800-Mg-Fe	0	7.7	
800-Cu5-Mg-Fe	0.3	8.6	46
800-Cu7-Mg-Fe	0.5	9.0	54
800-Cu10-Mg-Fe	0.7	8.7	56
800-Cu12-Mg-Fe	0.9	9.1	60
800-Cu15-Mg-Fe	0.9	8.8	57
800-Mg-Fe-Ce	0	8.2	
800-Cu5-Mg-Fe-Ce	0.3	8.5	45
800-Cu7-Mg-Fe-Ce	0.5	9.5	57
800-Cu10-Mg-Fe-Ce	0.7	10.1	62
800-Cu12-Mg-Fe-Ce	0.8	9.9	61
800-Cu15-Mg-Fe-Ce	0.9	9.3	63

\* calculated on the basis of XRF results and assumption that Cu is present only in Cu<sup>2+</sup> form.

The splitting of the low-temperature range peak registered for 800-Cu5-Mg-Fe-Ce could be related to two-step reduction of Cu: (i) CuO→Cu<sub>2</sub>O and (ii) Cu<sub>2</sub>O→Cu [25]. Additional peaks assigned to copper reduction were found at a temperature about 580 °C, and represented the reduction of Cu<sup>2+</sup> cations located in Cu<sub>x</sub>Mg<sub>1-x</sub>Fe<sub>2</sub>O<sub>4</sub> oxides (Cu<sup>2+</sup>→Cu) [49]. The reduction of Fe ranged from 400–900 °C with maxima at about 500, 700 and 780 °C. In the case of all catalysts, iron reduction occurs in a multi-step way. The maximum at the lowest temperature (about 500 °C) could be ascribed to the reduction of Fe<sub>2</sub>O<sub>3</sub> small particles to FeO (Fe<sub>2</sub>O<sub>3</sub>→FeO) and/or Fe<sub>2</sub>O<sub>3</sub> to Fe<sub>3</sub>O<sub>4</sub>. For the catalysts containing copper, the reduction maximum at about 500 °C shifts to higher temperatures with the increase of copper loading, which is related to the Cu location in the spinel-type structure, and therefore, more difficult reduction of Fe [50,51]. The shift of this maximum was observed for both series of catalysts. Reduction maxima observed at higher temperatures are related to the reduction of Fe<sub>2</sub>O<sub>3</sub> to Fe (about 700 °C) and FeO to Fe (about 780 °C) [50,51]. The maximum at higher temperature could be observed in profiles registered for 800-Cu15-Mg-Fe, 800-Cu15-Mg-Fe-Ce and reference materials. Both maxima assigned to Fe<sub>2</sub>O<sub>3</sub> and FeO are related to iron located in the spinel-like structure.

Further analysis of the presented H<sub>2</sub>-TPR curves allows observing that the maxima at approximately 500 °C for catalysts containing lower amounts of copper are shifted to lower temperatures in comparison to reference samples (800-Mg-Fe and 800-Mg-Fe-Ce). It could be assumed that the formed

$\text{Cu}^{2+}\text{-O-Fe}^{3+}$  species in the  $\text{Cu}_x\text{Mg}_{1-x}\text{Fe}_2\text{O}_4$  oxide are easier to reduce than  $\text{Fe}^{3+}\text{-O-Fe}^{3+}$  species in a pure  $\text{MgFe}_2\text{O}_4$  structure [49]. A similar effect has been reported for other Cu-Ce based catalysts [18,25,50]; however, this effect was not observed for the presented catalysts.  $\text{CeO}_2$  reduction is expected to proceed at around 800 °C and cannot be differentiated from the complex Fe oxides reduction profile.

From the  $\text{H}_2$  consumption results, it is visible that copper addition caused an increase of hydrogen consumption as expected, but with the increasing amount of copper, no substantial increase of total  $\text{H}_2$  consumption took place. Since copper oxide is reducible in the studied temperature range and there was no copper in  $\text{Cu}^0$  form visible in XRD results, it means that copper incorporation into the catalyst was accompanied by compensating changes of oxidation states of iron. However, there was a clear trend regarding the reduction of individual copper phases: With increasing copper amount in samples up to 10 mol %, the amount of copper reducible in the low temperature region increased, as well as the amount of copper reducible in the higher temperature region (Figure 5, Table 7). However, when a higher amount of copper was present, a significant rearrangement of phases took place, and the reduction profiles changed significantly, which is in accordance with the results of XRD, as well as the  $\text{N}_2$  physisorption measurements, cyclic voltammetry and UV-vis.

The redox properties of prepared catalysts were studied by cyclic voltammetry (CV). Cyclic curves of chosen catalysts (800-Cu5-Mg-Fe, 800-Cu5-Mg-Fe-Ce, 800-Cu12-Mg-Fe and 800-Cu12-Mg-Fe-Ce) are presented in Figure 6. CV curves for the rest of the samples can be found in Supplementary, Figures S2 and S3. The presented voltammograms (Figure 6) allow observing the quasi-reversible nature of red-ox processes that occur on individual materials. The registered signals are related to copper redox cycles: The upper curve maxima are related to  $\text{Cu}^0 \rightarrow \text{Cu}^{2+}$  oxidation process (OX), while the bottom curve maxima are related to  $\text{Cu}^{2+} \rightarrow \text{Cu}^0$  reduction (RED). Redox cycles characteristic for  $\text{Fe}^0 \rightarrow \text{Fe}^{3+} \rightarrow \text{Fe}^0$  are expected at a higher potential range [52–54]; however, due to limitations of prepared graphite paste and its unstable nature at higher potentials, these redox cycles were not registered. The additional signal observed at the upper curve for 800-Cu5-Mg-Fe-Ce sample is related to the formation of another Cu form that is easier to oxidize than  $\text{Cu}^{2+}$  cations. On the basis of previously presented  $\text{H}_2$ -TPR results, this signal could be ascribed to  $\text{Cu}^+ \rightarrow \text{Cu}^{2+}$ ; however, because the intensity of this maximum decrease with the increasing number of red-ox cycles and the corresponding reduction wave is not observed at bottom curve, this process is irreversible, and the  $\text{Cu}^+$  forms are not re-formed after oxidation to  $\text{Cu}^{2+}$ . The intensity of the main OX and RED signals registered for 800-Cu5-Mg-Fe and 800-Cu5-Mg-Fe-Ce samples change during each red-ox cycle. At the beginning of the measurements, the intensity of OX signal and  $I_{\text{OX}}/I_{\text{RED}}$  ratio increased, which means that more  $\text{Cu}^{2+}$  are formed in relation to  $\text{Cu}^0$ . With the increasing number of the cycles, the intensity of OX signal (current, mA) and  $I_{\text{OX}}/I_{\text{RED}}$  ratio decreased and become closer to 1, which means that red-ox processes become more reversible. For the samples with higher Cu amount 800-Cu12-Mg-Fe and 800-Cu12-Mg-Fe-Ce, the  $I_{\text{OX}}/I_{\text{RED}}$  ratio is much higher in relation to samples with lower Cu amount. It could be seen that with each red-ox cycle, the amount of  $\text{Cu}^{2+}$  cations increased in relation to the  $\text{Cu}^0$  cations amount.

For samples with a lower copper amount, the oxidation maximum of the first red-ox cycle was found at about 70 mV. Increasing the number of cycles caused a shift of potential to higher values—96 mV for 800-Cu5-Mg-Fe and 88 mV for 800-Cu5-Mg-Fe-Ce, which is related to more difficult oxidation of samples in comparison with the first cycle. However, it should be noted that the last cycle (20th cycle) for both samples is characterized by a maximum at about 80 mV, which means that with each cycle, the samples became easier to oxidize. A similar potential shift from –137 mV to –95 mV for 800-Cu5-Mg-Fe and from –130 mV to –90 mV for 800-Cu5-Mg-Fe-Ce is observed for reduction potential (lower curves). On the basis of these observations, it could be assumed that with an increasing number of red-ox cycles, the samples became easier to reduce.

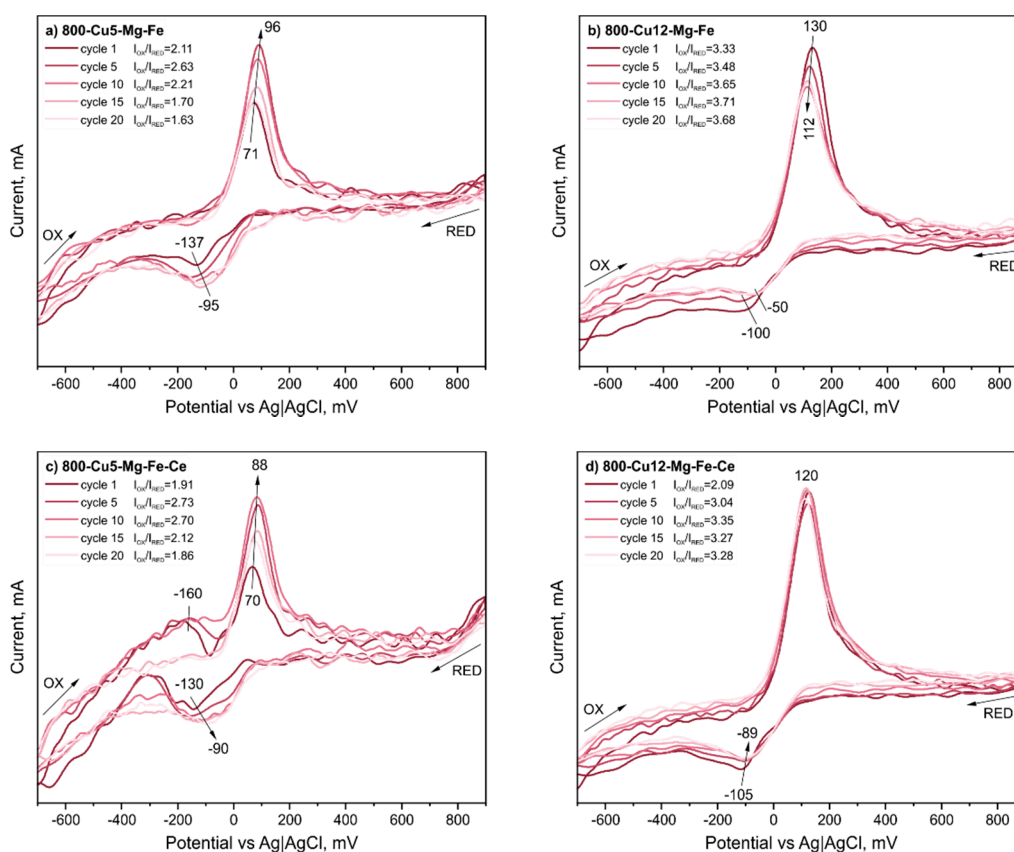


**Figure 6.** CV multi-cyclic curves registered for catalysts (a) 800-Cu5-Mg-Fe, (b) 800-Cu12-Mg-Fe, (c) 800-Cu5-Mg-Fe-Ce, (d) 800-Cu12-Mg-Fe-Ce; OX—oxidation curve, RED—reduction curve; direction of potential change for OX and RED curves is described by arrows;  $I_{OX}$ ,  $I_{RED}$ —intensity of oxidation and reduction signal, respectively.

In the case of samples with a higher copper amount, the oxidation and reduction potential is shifted to higher values in comparison to samples with lower copper loading—130 mV (OX) and −130 mV (RED) for 800-Cu12-Mg-Fe and 120 mV (OX) and −100 mV (RED) for 800-Cu12-Mg-Fe-Ce, which means that these samples are more difficult to oxidize and easier to reduce than 800-Cu5-Mg-Fe and 800-Cu5-Mg-Fe-Ce. Moreover, it could also be observed that for both samples, with the increasing number of red-ox cycles, the reduction potential shifted to higher values (−50 mV for 800-Cu12-Mg-Fe and to −89 mV for 800-Cu12-Mg-Fe-Ce), meaning that both catalysts became easier to reduce. The oxidation potential of 800-Cu12-Mg-Fe shifts to a lower value, approximately 112 mV, which indicates that this material became easier to oxidize. CV curves allow us to conclude that oxidation states in the case of samples with a higher copper amount are more stable than for catalysts with lower Cu-loading.

The significant differences of shape and intensity of OX and RED signals could be observed at multi-cyclic curves registered for sample 800-Cu15-Mg-Fe (Supplementary, Figure S2). The low intensity of the OX and RED maxima at cycle 1 suggest that red-ox processes are difficult, what could be related to the accessibility of  $\text{Cu}^{2+}$  cations on the material surface. In the case of sample 800-Cu15-Mg-Fe-Ce (Supplementary, Figure S3), the first cycle also suggests limited accessibility of  $\text{Cu}^{2+}$  cations on the surface; however, the significant increase of the OX signal observed for this material suggested that  $\text{Cu}^{2+}$  cations are formed with each redox cycle.

### 2.3. Catalytic Studies

The  $\text{NH}_3$  removal and selectivity to  $\text{N}_2$  over 800-Cu5-Mg-Fe, 800-Cu12-Mg-Fe, 800-Cu5-Mg-Fe-Ce and 800-Cu12-Mg-Fe-Ce samples as a function of time for isothermal long term (180 min) states at temperatures 200, 250, 300 and 350 °C are shown in Figure 7. The chosen samples represent general trends characteristic for both series of materials. On the basis of presented results, it can be seen that the 800-Cu5-Mg-Fe and 800-Cu12-Mg-Fe catalysts are inactive below 300 °C (Figure 7a), while the 800-Cu5-Mg-Fe-Ce and 800-Cu12-Mg-Fe-Ce catalysts are inactive below 250 °C (Figure 7b). At higher temperatures, both series of materials become active as catalysts of the  $\text{NH}_3$ -SCO process. Further increase in temperature causes a significant increase of catalytic efficiency; however, neither catalysts modified by Ce nor catalysts unmodified by Ce reach total ammonia conversion. The best removal efficiency, about 70%, at 350 °C was observed for samples with 12 mol % of copper loading. For the 800-Cu12-Mg-Fe and 800-Cu12-Mg-Fe-Ce catalysts, selectivity to dinitrogen at 350 °C reaches about 75%. For the samples with lower copper loading, 800-Cu5-Mg-Fe and 800-Cu5-Mg-Fe-Ce, the determination of  $\text{NH}_3$  removal efficiency and selectivity to dinitrogen is clearly impossible, because of the absence of ammonia and nitrogen plateaus at 350 °C (Figure 7), which is in accordance with the results of cyclic voltammetry. However, maximum levels of ammonia removal at 350 °C that were registered during the 180 min heating period for these catalysts are 56% and 46% for 800-Cu5-Mg-Fe and 800-Cu5-Mg-Fe-Ce, respectively. It could be expected that further increase in temperature should cause an increase of  $\text{NH}_3$  removal and a decrease in selectivity to  $\text{N}_2$ . Comparison of the obtained results with a removal efficiency of the 800-Mg-Fe sample, which was almost inactive ( $\text{NH}_3$  conversion at 350 °C was 3%, results not shown.) allow assuming that Cu-based species are responsible for catalysts activity at low temperature range.

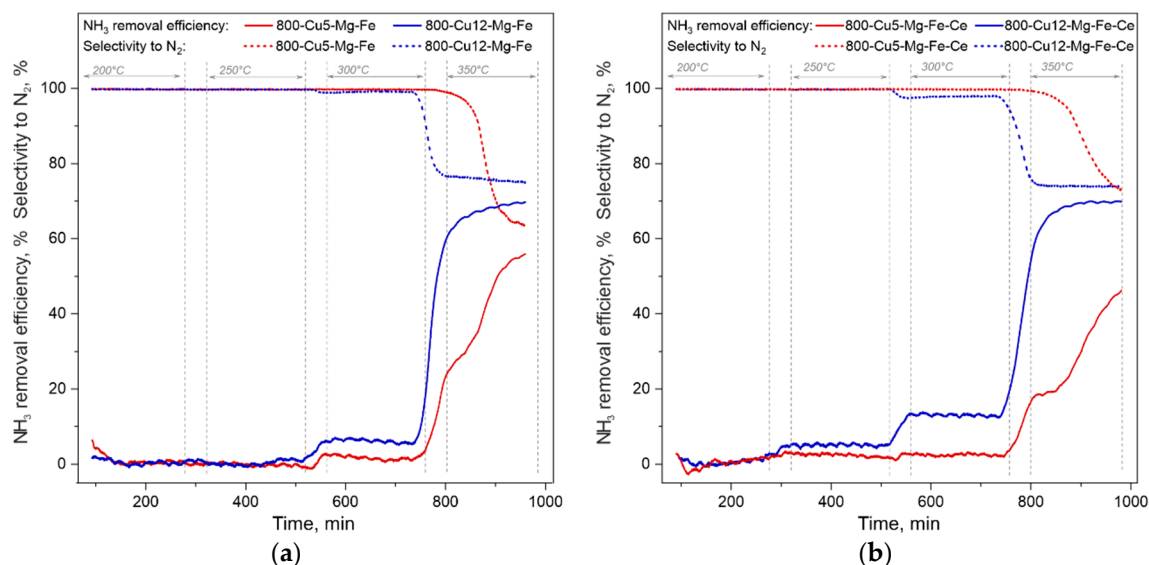


**Figure 7.** Results of selective catalytic oxidation of ammonia to dinitrogen over (a) 800-Cu5-Mg-Fe and 800-Cu12-Mg-Fe catalysts; (b) 800-Cu5-Mg-Fe-Ce and 800-Cu12-Mg-Fe-Ce; solid line—ammonia removal efficiency (%), dotted line - selectivity to dinitrogen (%); temperature ranges marked by a vertical, dotted gray line.

The results of selective catalytic oxidation of ammonia and selectivity to  $\text{N}_2$ ,  $\text{NO}$ ,  $\text{N}_2\text{O}$ ,  $\text{NO}_2$  obtained at 350 °C in steady state for all copper-based catalysts are presented in Figure 8. The presented results show that the 800-Cu15-Mg-Fe and 800-Cu15-Mg-Fe-Ce samples are characterized by the lowest  $\text{NH}_3$  removal efficiency of approximately 18% and 8%, respectively. The removal efficiency of the 800-Cu5-Mg-Fe-Ce, 800-Cu7-Mg-Fe-Ce and 800-Cu10-Mg-Fe-Ce catalysts are similar, approximately 45%, while the removal efficiency of 800-Cu12-Mg-Fe-Ce is much higher and reaches 75%. It could be

seen that in the case of Ce-doped samples (apart of 800-Cu15-Mg-Fe-Ce), over 70% of oxidation products is nitrogen. The comparison of samples with lower copper amount shows that the non-modified 800-Cu5-Mg-Fe and 800-Cu7-Mg-Fe catalysts are characterized by higher  $\text{NH}_3$  removal efficiency (above 55%); however, the selectivity to dinitrogen over these catalysts is about 10% lower in relation to 800-Cu5-Mg-Fe-Ce and 800-Cu7-Mg-Fe-Ce. Lower  $\text{N}_2$  selectivity results in a higher level of NO and  $\text{NO}_2$  concentration. Only an insignificant amount of  $\text{N}_2\text{O}$  was observed over all catalysts.

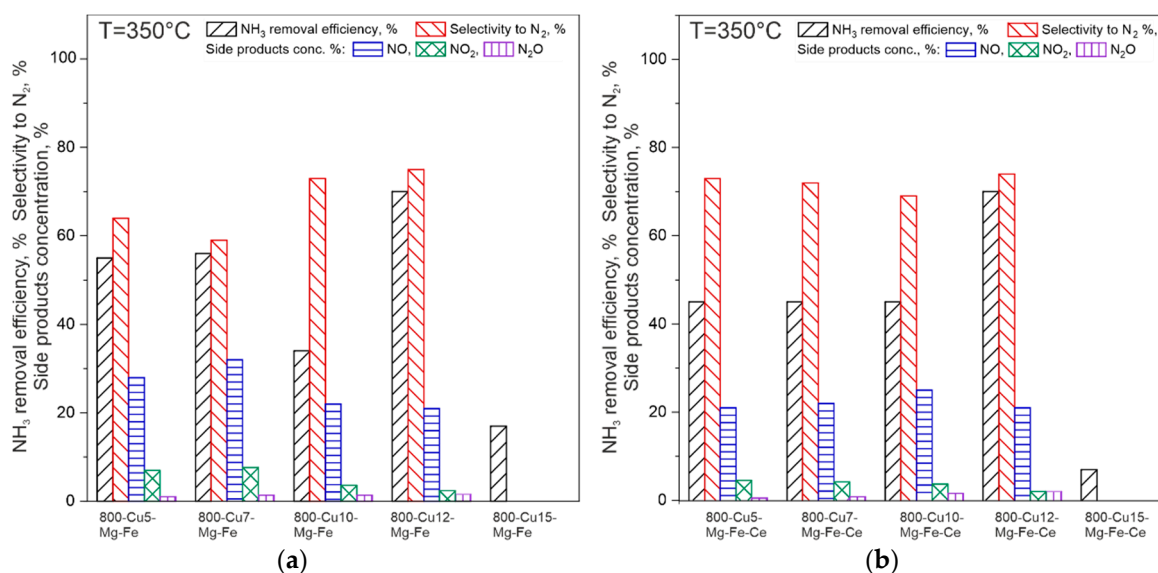


**Figure 8.** Results of selective catalytic oxidation of ammonia to dinitrogen at 350 °C over (a) 800-Cu-Mg-Fe-O catalysts; (b) 800-Cu-Mg-Fe-O-Ce catalysts.

In catalysis, the specific surface area of catalysts is often considered as one of the most important attributes that affect the catalytic efficiency of tested materials. In our case, the dependence of activity and selectivity on the  $S_{\text{BET}}$  surface area was not observed. Therefore, the results of  $\text{NH}_3$ -oxidation (ammonia removal efficiency and selectivity to main and side products) are rather related to phase composition and redox properties than to textural properties.

It was shown that the obtained oxides exhibit quasi-reversible nature during redox processes which could be related to the formation of  $\text{Cu}^{2+}\text{-O-Fe}^{3+}$  [49] and  $\text{Cu}^{2+}\text{-O-Ce}^{4+}$  [55,56] couples on the surface of catalysts. The occurrence of  $\text{Cu}^{2+}\text{-O-Fe}^{3+}$  and  $\text{Cu}^{2+}\text{-O-Ce}^{4+}$  redox couples on the surface of catalysts could influence the redox properties and reducibility of calcined catalysts. Changing of these properties could favor the generation of oxygen vacancies. A similar effect has been reported by Shi et al. [49] who studied the synergistic coexistence of Cu-Fe catalytic systems modified by Mn, Tang et al. [56] who reported the redox properties and catalytic behavior of  $\text{CuO/CeO}_2$  and Wang et al. [50] who studied the effect of Ce addition on  $\text{Cu}_x\text{Ce}_{1-x}\text{Fe}_2\text{O}_4$  catalytic properties. All authors point out that both iron and ceria located close to Cu influence its oxidation states and change its catalytic properties. Reduction of these couples could generate oxygen vacancies ( $\text{Cu}^+\text{-O-Fe}^{2+}$  and  $\text{Cu}^+\text{-O-Ce}^{3+}$  [55,56]) that could easily react with ammonia and/or the side products of the  $\text{NH}_3$ -SCO reaction ( $\text{NO}$ ,  $\text{N}_2\text{O}$ ,  $\text{NO}_2$ ) to nitrogen. In the case of 800-Cu5-Mg-Fe-Ce and 800-Cu7-Mg-Fe-Ce, the increase of selectivity to nitrogen in comparison to non-modified samples could be related to the formation of  $\text{Cu}^{2+}\text{-O-Ce}^{4+}$ .

Cu-based oxides are known as efficient catalysts of selective catalytic oxidation of ammonia. It has been reported [9,10,15,21] that for Cu-based catalysts containing more than 10 wt. % of Cu, ammonia conversion increases, while  $\text{N}_2$  selectivity decreases (to approximately 30–50%). These effects should be expected, due to the occurrence of side reactions. In the case of the presented catalysts, a decrease of selectivity to nitrogen with increased copper loading was not observed, however, with copper overloading (more than 12 wt. %), a steep drop in  $\text{NH}_3$  conversion was observable. It was supposed

that such behavior could be explained by specific phase composition and structure morphology of the obtained catalysts.

Characterization of calcined samples showed the formation of distinguishable non-stoichiometric  $\text{Cu}_x\text{Mg}_{1-x}\text{Fe}_2\text{O}_4$  with increasing copper loading accompanied by a continual increase of pure copper oxide phase only up to 12 wt. % copper level. The mixed metal oxides (especially obtained by calcination at high temperatures) are expected to present heterogeneous structure. Heterogeneous nature of all catalysts was confirmed, and for that reason, solely heterogeneous structure of catalysts should not be connected with steep change and the poor activity of 800-Cu15-Mg-Fe and 800-Cu15-Mg-Fe-Ce samples. However, the degree of heterogeneity, crystallinity and dispersion of individual phases showed obvious trends and progress with increasing Cu amount in the samples and indicates the presence of different structure for 800-Cu15-Mg-Fe and 800-Cu15-Mg-Fe-Ce samples. Despite the fact that all characterization techniques showed steep changes in catalyst properties when reaching the critical value of copper amount (i) the SEM observations (Figures 2 and 3) there are visible Cu rich species which are not observable in samples with lower Cu amount, (ii) the  $\text{H}_2$ -TPR- $\text{H}_2$  results (Figures 4 and 5 and Table 7) point out rearrangement of the phases from the point of view of oxidation states, as well as crystallinity and dispersion; (iii) the same conclusion can be visible from  $\text{N}_2$  physisorption (Table 6), cyclic voltammetry (Figure 6) and XRD measurements (Figure 1, Table 5)). None of these explicitly expressed properties was found out to be directly responsible for the activity, and no straightforward linkage to the specific phase type was observed.

Data presented in Table 7 and Figure 5 guided us to connect the catalytic activity with the formation of CuO species. The pct. of total Cu amount reduced at a low-temperature range was higher for samples with high Cu amount which means that for samples enriched by copper, a formation of CuO simple oxide is favored instead of Cu incorporation in spinel network. However, when comparing activity and  $\text{H}_2$ -TPR results, the 800-Cu15-Mg-Fe and 800-Cu15-Mg-Fe-Ce samples have similar low-temperature reduction degree to the 800-Cu12-Mg-Fe and 800-Cu12-Mg-Fe-Ce ones (0.9), which cannot explain almost zero activity of the Cu15 samples. It is well-known from the literature that in the case of  $\text{NH}_3$ -SCO catalysts, the highly dispersed and easily reducible CuO species are more active and efficient than bulk-like. This activation effect is related to the formation of  $[\text{Cu-O-Cu}]^{2+}$  species [9]. For that reason, based on literature results and implicitly deduced from our results, we suppose that only CuO in highly dispersed form is mainly responsible for the activity and the activity is, thus, connected to decrease in the dispersion and formation of bulk-like CuO species probably resulting in the decrease in copper oxide specific surface area. Unfortunately, we were not able to distinguish what part of CuO in our samples is in “highly dispersed form”. On the basis of multi-cyclic curves (Supplementary, Figures S2 and Figure S3) it could be assumed that in the case of samples 800-Cu15-Mg-Fe and 800-Cu15-Mg-Fe-Ce, accessibility of  $\text{Cu}^{2+}$  surface cations are difficult compared to other samples, what could be related to the formation of bulk-like species.

Cu-Mg-Fe mixed metal oxides systems obtained by calcination of hydrotalcite-like materials and their catalytic efficiency as catalysts of  $\text{NH}_3$ -SCO process were studied previously in the literature. Chmielarz et al. [15] presented the catalytic efficiency of Cu-Mg-Fe mixed metal oxides calcined at 600 °C. They have reported that such catalysts are characterized by a conversion of about 80% with  $\text{N}_2$  selectivity of approximately 90–95% (at 350 °C), while total conversions of  $\text{NH}_3$  were observed at a higher temperature range 400–450 °C. In comparison to materials presented by us, hydrotalcite calcination temperature lower than 800 °C seems to be more optimal for the  $\text{NH}_3$ -SCO process. The effect of calcination temperature on the catalytic efficiency of Cu-Mg-Fe mixed metal oxides was studied by Jabłońska et al. [57]. It was shown that materials calcined at 900 °C are characterized by lower catalytic efficiency ( $\text{NH}_3$  conversion of about 60% and selectivity to  $\text{N}_2$  of about 95% at 350 °C) than materials obtained by calcination at 600 °C ( $\text{NH}_3$  conversion and  $\text{N}_2$  selectivity of about 95% at 350 °C). However, it should also be mentioned that materials obtained at lower temperatures in relation to materials calcined at higher temperatures are more susceptible to structural changes related to memory effect, due to lower crystallinity. Therefore, the addition of water vapour into the

flow of reactants could easily change the structure of these kinds of materials during the long-term exposition. This could result in a decrease in catalytic efficiency. Jabłońska et al. [57] also studied the thermal decomposition of Cu-Mg-Fe hydrotalcite-like materials. It was shown that with increasing calcination temperature, the crystallinity of catalysts increased and the phase composition of the obtained materials became more diverse. The  $\text{CuFe}_2\text{O}_4$  spinel structures characterized by different surface area  $12 \text{ m}^2/\text{g}$  (SG-CuFe) and  $194 \text{ m}^2/\text{g}$  (MP-CuFe) were studied as catalysts of selective catalytic oxidation of ammonia to dinitrogen by Yue et al. [58]. Material with higher surface area presents very high catalytic activity at  $350 \text{ }^\circ\text{C}$  with the  $\text{NH}_3$  conversion level and  $\text{N}_2$  selectivity at about 98%, while SG-CuFe catalyst at the same temperature ( $\text{GHSV} = 1250 \text{ mL min}^{-1} \text{ g}^{-1}$ ) represents lower  $\text{NH}_3$  conversion (40%) and  $\text{N}_2$  selectivity (96%). It seems that the activity of these samples is related mainly to the surface area. Our most active mixed metal oxides 800-Cu12-Mg-Fe and 800-Cu12-Mg-Fe-Ce are characterized by small surface area below  $6.5 \text{ m}^2/\text{g}$  (Table 6). At the same time, the ammonia removal efficiency is almost two-times higher (70–73%;  $\text{GHSV} = 500 \text{ mL min}^{-1} \text{ g}^{-1}$ ) than SG-CuFe presented by Yue et al. [58].

According to the mechanisms of ammonia oxidation described in the literature the most probable mechanisms for Cu-Mg-Fe mixed metal oxides is the internal selective ammonia oxidation (i-SCR) that include oxidation of part of  $\text{NH}_3$  to NO and further NO reduction by  $\text{NH}_3$  to  $\text{N}_2$  [13,16,17]. Because of that, possible improvement of Cu-Mg-Fe catalysts activity could be reached by the modification of their surface by other metals (e.g., noble metals, [16–19,59]) that are responsible for selective oxidation of ammonia to NO [60] and ensuring the accessibility of active species by structural promoters, e.g., aluminum [14,21,57,61].

### 3. Conclusions

The aim of the presented work was to study the efficiency of Cu-Mg-Fe-O and Cu-Mg-Fe-O-Ce mixed metal oxides obtained by calcination of hydrotalcite-like materials at  $800 \text{ }^\circ\text{C}$  as catalysts for selective catalytic oxidation of ammonia to dinitrogen. The thermal transformation process of hydrotalcite-like materials into metal oxides resulted in obtaining a mixture of oxides characterized by simple and complex oxide structures with relatively low surface area (below  $35 \text{ m}^2/\text{g}$ ). Characterization results revealed that the discussed catalysts are composed of CuO, MgO, (Cu)MgFe<sub>2</sub>O<sub>4</sub>-type and CeO<sub>2</sub> (in the case of the Ce-doped samples) structures. All samples below 12 wt % copper loading were active at a low-temperature range (up to  $350 \text{ }^\circ\text{C}$ ) and displayed high selectivity to  $\text{N}_2$ . As expected, the  $\text{NH}_3$  conversion level increased with increasing copper loading. Activity and selectivity to dinitrogen could be related to the formation of Cu-Fe and Cu-Ce species that can generate oxygen vacancies and favors the oxidation of ammonia to dinitrogen. The most active samples exhibited relatively high  $\text{N}_2$  selectivity (about 75%), which means that further modification of Cu-Mg-Fe based oxide systems in order to improve their efficiency, while maintaining high selectivity of  $\text{NH}_3$ -SCO process is possible.

### 4. Materials and Methods

#### 4.1. Catalysts Preparation

Precursors of mixed metal oxides, hydrotalcite-like materials with the intended Cu/Mg/Fe chemical compositions (mol % of total metals amount) 5/62/33 (HT-Cu5-Mg-Fe), 7/60/33 (HT-Cu7-Mg-Fe), 10/57/33 (HT-Cu10-Mg-Fe), 12/55/33 (HT-Cu12-Mg-Fe), 15/52/33 (HT-Cu15-Mg-Fe) and 0/67/33 (HT-Mg-Fe) were synthesized by the co-precipitation method from aqueous solutions of:  $\text{Cu}(\text{NO}_3)_2 \cdot 6\text{H}_2\text{O}$  (Penta),  $\text{Mg}(\text{NO}_3)_2 \cdot 6\text{H}_2\text{O}$  (Penta),  $\text{Fe}(\text{NO}_3)_3 \cdot 9\text{H}_2\text{O}$  (Penta) (total concentration  $1.0 \text{ mol L}^{-1}$ ). Metal concentrations were chosen to obtain  $\text{M}^{2+}/\text{M}^{3+}$  ratio of 2.03, which should result in the formation of a well-developed layered structure. The higher amount of  $\text{Fe}^{3+}$  could result in the formation of iron hydroxide precipitates. Nitrate solutions were added dropwise, simultaneously with an alkaline solution of NaOH ( $c = 3.0 \text{ mol L}^{-1}$ ) and  $\text{Na}_2\text{CO}_3$  ( $c = 0.5 \text{ mol L}^{-1}$ ) into a heated reactor containing distilled water (200 mL). The flow rate of cation solutions was fixed at approximately  $8 \text{ mL min}^{-1}$ , while the flow rate



of the precipitation solution ( $\text{NaOH} + \text{Na}_2\text{CO}_3$ ) was controlled by a pH controller and added as needed to establish the precipitate pH at about  $\text{pH} = 10.0 \pm 0.2$ . The synthesis was carried out under vigorous stirring at  $60\text{ }^\circ\text{C}$  until the cation solution was completely consumed. The obtained precipitate was aged at  $60\text{ }^\circ\text{C}$  for 1 h under vigorous stirring. The obtained product was filtered, washed with distilled water and dried at  $60\text{ }^\circ\text{C}$  in air for at least 10 h. The dried samples were crushed to powder with grain size lower than  $0.125\text{ }\mu\text{m}$ .

Cu-Mg-Fe-O mixed metal oxides were obtained by the calcination of synthesized precursors at  $800\text{ }^\circ\text{C}$  for 9 h in air. After calcination, part of the obtained products was additionally doped by cerium (5 wt %, 2.5 mol %) using the wet impregnation method and re-calcined to obtain the Cu-Mg-Fe-O-Ce mixed metal oxides. A pure  $\text{Ce}(\text{NO}_3)_3 \cdot 6\text{H}_2\text{O}$  (Penta) solution was used for impregnation. After impregnation, the samples were dried at  $60\text{ }^\circ\text{C}$  for about 12 h and re-calcined at  $800\text{ }^\circ\text{C}$  in air for 9 h. Sample codes and intended compositions are shown in Table 2.

#### 4.2. Sample Characterization

The phase composition of the hydrotalcite-like materials and the obtained 800-Cu-Mg-Fe-O, 800-Cu-Mg-Fe-O-Ce oxide systems were determined by X-ray diffraction. Diffractograms were recorded using a Rigaku Smart Lab diffractometer using  $\text{Co K}\alpha$  radiation ( $\lambda = 0.179\text{ nm}$ ) in the range of  $5$  to  $90\text{ }^\circ 2\theta$  with a step size of ( $0.01\text{ }^\circ 2\theta$ ). Quantitative analysis was performed with the use of dedicated software and compared with the ICDD database.

The FT-IR spectra of as-synthesized hydrotalcite-like materials were measured by a Nicolet 740 FT-IR (Thermo Scientific) spectrometer. The measurements were carried out in the range  $500\text{--}4000\text{ cm}^{-1}$  with a resolution of  $2\text{ cm}^{-1}$ .

The UV-Vis diffuse reflectance spectroscopy spectra (DRS) of the calcined samples were recorded with a Shimadzu UV-2600 (IRS-2600Plus) spectrophotometer. The measurements were performed in the range of  $220$  to  $1400\text{ nm}$  with a resolution of  $1\text{ nm}$ . The optical direct band gap was estimated on the basis of the first linear region of Tauc's plot.

The morphology of calcined catalysts was determined by scanning electron microscopy (SEM) using an FEI Quanta 450 with secondary electrons (SE) and backscattered electrons (BSE) mode. Prior to the measurements, the samples were sputtered with gold.

The specific surface area of the calcined samples was determined by the BET method using a 3Flex (Micromeritics) automated gas adsorption system. Prior to the nitrogen adsorption at  $-196\text{ }^\circ\text{C}$ , all samples were outgassed in vacuum at  $350\text{ }^\circ\text{C}$  for 24 h.

The reducibility of mixed metal oxides was studied by temperature-programmed reduction ( $\text{H}_2$ -TPR) using an AutoChem II 2920 (Micromeritics). The experiments were carried out in a fixed-bed flow microreactor at temperature range  $40\text{--}900\text{ }^\circ\text{C}$  with a temperature increase rate of  $20\text{ }^\circ\text{C min}^{-1}$  in a flow ( $50\text{ mL min}^{-1}$ ) of  $10\%$   $\text{H}_2$  diluted in Ar. Prior to the measurements, samples were outgassed in a flow of Ar ( $50\text{ mL min}^{-1}$ ) at  $750\text{ }^\circ\text{C}$  for 60 min and cooled down to  $40\text{ }^\circ\text{C}$  in the same gas atmosphere.

The redox properties of calcined samples were recorded in a three-electrode cell using graphite paste electrode as the working electrode (WORK), platinum coil as the auxiliary electrode (AUX) and  $\text{Ag}|\text{AgCl}$  as the reference electrode (REF). The composite paste was prepared by mixing synthetic graphite ( $100\text{--}150\text{ mg}$ ) with Njuol ( $0.05\text{--}0.1\text{ mL}$ ) and a small amount of solid catalyst (about  $5\text{ mg}$ ). The obtained paste was well-packed into the electrode. The measurements were performed in an acetate buffer ( $\text{pH} = 4.6$ ) mixed with distilled water in proportion 1:3 as electrolyte at a scan rate of  $50\text{ mV s}^{-1}$  and potential window  $-700$  to  $900\text{ mV}$ . Before each experiment, the solution was pretreated with argon to keep an oxygen-free atmosphere during measurement.

#### 4.3. Catalytic Studies

Selective catalytic oxidation of ammonia was performed in a fixed-bed flow-through quartz microreactor system (microreactor inner diameter of  $4\text{ mm}$ ) under atmospheric pressure at a temperature range of  $200$  to  $350\text{ }^\circ\text{C}$  with an isothermal step every  $50\text{ }^\circ\text{C}$ . Every temperature step lasted 180 min.

For each test, 200 mg of catalyst was used. Prior to the measurements, the samples were activated in air flow ( $100 \text{ mL min}^{-1}$ ) at  $200 \text{ }^\circ\text{C}$  for 60 min. After that, a mixture of 0.25 mol %  $\text{NH}_3$  diluted in He ( $10 \text{ mL min}^{-1}$ ) and synthetic air were supplied into the reactor (total air flow  $100 \text{ mL min}^{-1}$ ). Ammonia concentration in the gas mixture was established at 350 ppm.

Ammonia and the products of a catalytic reaction—nitric oxide (NO), nitrogen dioxide ( $\text{NO}_2$ ), nitrous oxide ( $\text{N}_2\text{O}$ ) and water vapor were detected by FT-IR (Antaris IGS, Nicolet). Ammonia conversion was calculated with the use of Equation (1):

$$(\text{NH}_3)_{\text{conv}} = \left( \frac{[\text{NH}_3]_{\text{in}} + [\text{NH}_3]_{\text{out}}}{[\text{NH}_3]_{\text{in}}} \right) \cdot 100(\%). \quad (1)$$

Process selectivity to the dinitrogen was calculated with the use of Equation (2):

$$(\text{N}_2)_{\text{sel}} = \left( 1 - \frac{[\text{NO}]_{\text{out}} + [\text{NO}_2]_{\text{out}} + 2[\text{N}_2\text{O}]_{\text{out}}}{[\text{NH}_3]_{\text{in}} - [\text{NH}_3]_{\text{out}}} \right) \cdot 100(\%). \quad (2)$$

Process selectivity to side products was calculated with the use of Equation (3):

$$\text{Sel}_i = \frac{[\text{C}_i]_{\text{out}}}{\sum [\text{C}_i]_{\text{out}}}. \quad (3)$$

**Supplementary Materials:** The following are available online at <http://www.mdpi.com/2073-4344/10/2/153/s1>, Figure S1: Results of the characterization of HT-Cu-Fe samples (a) XRD phase analysis (b) infrared spectroscopy measurements, Figure S2: CV multi-cyclic curves registered vs Ag|AgCl electrode at potential window from -700 to 900 mV at acetate buffer (pH=4.6) for 800-Cu-Mg-Fe-O catalysts; OX – oxidation curve, RED – reduction curve; direction of potential change for OX and RED curves is described by arrows, Figure S3: CV multi-cyclic curves registered vs Ag|AgCl electrode at potential window from -700 to 900 mV at acetate buffer (pH=4.6) for 800-Cu-Mg-Fe-O-Ce catalysts; OX – oxidation curve, RED – reduction curve; direction of potential change for OX and RED curves is described by arrows.

**Author Contributions:** Conceptualization S.G. and K.P. (Kateřina Pacultová); methodology, S.G.; investigation, S.G., A.S., K.G., K.P. (Katarzyna Pamin); writing—original draft preparation, S.G.; writing—review and editing, K.P. (Kateřina Pacultová), L.O.; supervision, L.O., visualization, S.G., K.P. (Kateřina Pacultová); project administration L.O., K.P. (Kateřina Pacultová). All authors have read and agreed to the published version of the manuscript.

**Funding:** This work was supported by EU structural funding in Operational Programme Research, Development and Education, project No. CZ.02.1.01./0.0/0.0/17\_049/0008419 “COOPERATION”. Experimental results were accomplished by using Large Research Infrastructure ENREGAT supported by the Ministry of Education, Youth and Sports of the Czech Republic under project No. LM2018098.

**Acknowledgments:** The authors are grateful to Dagmar Fridrichová for  $\text{H}_2$ -TPR, Alexandr Martaus for XRD analyses, Lenka Matějová and Eva Kinnertová for nitrogen physisorption analyses.

**Conflicts of Interest:** The authors declare no conflict of interest. The funders had no role in the design of the study; in the collection, analyses, or interpretation of data; in the writing of the manuscript, or in the decision to publish the results.

## Abbreviations

### List of symbols

$(\text{NH}_3)_{\text{conv}}$	ammonia removal efficiency (conversion), %
$[\text{NH}_3]_{\text{in}}$	inlet ammonia concentration,
$[\text{NH}_3]_{\text{out}}$	outlet ammonia concentration
$(\text{N}_2)_{\text{sel}}$	selectivity to dinitrogen,
$[\text{NO}]_{\text{out}}$	outlet NO concentration,
$[\text{NO}_2]_{\text{out}}$	outlet NO <sub>2</sub> concentration,
$[\text{N}_2\text{O}]_{\text{out}}$	outlet N <sub>2</sub> O concentration.
$\text{Sel}_i$	selectivity to the side product i = NO, NO <sub>2</sub> or N <sub>2</sub> O,
$[\text{C}_i]_{\text{out}}$	outlet concentration of product i
$\Sigma [\text{C}_i]_{\text{out}}$	sum of outlet product concentrations, including N <sub>2</sub> concentration described as: $[\text{N}_2] = ([\text{NH}_3]_{\text{in}} - [\text{NH}_3]_{\text{out}} - [\text{NO}]_{\text{out}} - [\text{NO}_2]_{\text{out}} - 2[\text{N}_2\text{O}]_{\text{out}}) / 2$

## References

- Dammers, E.; McLinden, C.A.; Griffin, D.; Shephard, M.W.; Van Der Graaf, S.; Lutsch, E.; Schaap, M.; Gainairu-Matz, Y.; Fioletov, V.; Van Damme, M.; et al. NH<sub>3</sub> emissions from large point sources from CrIS and IASI satellite observations. *Atmos. Chem. Phys. Discuss.* **2019**, *19*, 1–47.
- Monteny, G.-J.; Hartung, E. *Ammonia Emissions in Agriculture*; Wageningen Academic Publishers: Wageningen, The Netherlands, 2007; ISBN 978-90-8686-0296.
- Borsari, V.; de Assunção, J.V. Ammonia emissions from a light-duty vehicle. *Transp. Res. Part D* **2017**, *51*, 53–61. [[CrossRef](#)]
- Sutton, M.A.; Reis, S.; Baker, S.M.H. *Atmospheric Ammonia. Detecting Emissions Changes and Environmental Impacts*; Sutton, M.A., Reis, S., Baker, S.M.H., Eds.; Springer: Dordrecht, The Netherlands, 2009; ISBN 9781402091209.
- Sutton, M.A.; Dragosits, U.; Hellsten, S.; Place, C.J.; Dore, A.J.; Tang, Y.S.; van Dijk, N.; Love, L.; Fournier, N.; Vieno, M.; et al. Ammonia emission and deposition in Scotland and its potential environmental impacts. *Sci. World Journal.* **2004**, *4*, 795–810. [[CrossRef](#)] [[PubMed](#)]
- NEC Directive Reporting Status 2015. 2015. Available online: <https://www.eea.europa.eu/themes/air/air-pollution-sources-1/national-emission-ceilings/nec-directive-reporting-status-2015> (accessed on 11 December 2019).
- Suarez-Bertoa, R.; Zardini, A.A.; Astorga, C. Ammonia exhaust emissions from spark ignition vehicles over the New European Driving Cycle. *Atmos. Environ.* **2014**, *97*, 43–53. [[CrossRef](#)]
- Elser, M.; El-Haddad, I.; Maasikmets, M.; Bozzetti, C.; Wolf, R.; Ciarelli, G.; Slowik, J.G.; Richter, R.; Teinmaa, E.; Hüglin, C.; et al. High contributions of vehicular emissions to ammonia in three European cities derived from mobile measurements. *Atmos. Environ.* **2018**, *175*, 210–220. [[CrossRef](#)]
- Chmielarz, L.; Jabłońska, M. Advances in selective catalytic oxidation of ammonia to dinitrogen: A review. *RSC Adv.* **2015**, *5*, 43408–43431. [[CrossRef](#)]
- Jabłońska, M.; Palkovits, R. Copper based catalysts for the selective ammonia oxidation into nitrogen and water vapour - recent trends and open challenges. *Appl. Catal. B Environ.* **2016**, *181*, 332–351. [[CrossRef](#)]
- FAO. *Global Estimates of Gaseous Emissions of NH<sub>3</sub>, NO and N<sub>2</sub>O from Agricultural Land*; FAO: Rome, Italy, 2001; ISBN 9251046891.
- Zawadzki, J. The mechanism of ammonia oxidation and certain analogous reactions. *Discuss. Faraday Soc.* **1950**, *8*, 140–152. [[CrossRef](#)]
- Zhang, X.; Wang, H.; Wang, Z.; Qu, Z. Adsorption and surface reaction pathway of NH<sub>3</sub> selective catalytic oxidation over different Cu-Ce-Zr catalysts. *Appl. Surf. Sci.* **2018**, *447*, 40–48. [[CrossRef](#)]
- Basąg, S.; Piwowarska, Z.; Kowalczyk, A.; Węgrzyn, A.; Baran, R.; Gil, B.; Michalik, M.; Chmielarz, L. Cu-Mg-Al hydrotalcite-like materials as precursors of effective catalysts for selective oxidation of ammonia to dinitrogen - The influence of Mg/Al ratio and calcination temperature. *Appl. Clay Sci.* **2016**, *129*, 122–130. [[CrossRef](#)]

15. Chmielarz, L.; Wegrzyn, A.; Wojciechowska, M.; Witkowski, S.; Michalik, M. Selective catalytic oxidation (SCO) of ammonia to nitrogen over hydrotalcite originated Mg-Cu-Fe mixed metal oxides. *Catal. Lett.* **2011**, *141*, 1345–1354. [CrossRef]
16. Zhang, L.; He, H. Mechanism of selective catalytic oxidation of ammonia to nitrogen over Ag/Al<sub>2</sub>O<sub>3</sub>. *J. Catal.* **2009**, *268*, 18–25. [CrossRef]
17. Wang, Z.; Qu, Z.; Quan, X.; Li, Z.; Wang, H.; Fan, R. Selective catalytic oxidation of ammonia to nitrogen over CuO-CeO<sub>2</sub> mixed oxides prepared by surfactant-templated method. *Appl. Catal. B Environ.* **2013**, *134–135*, 153–166. [CrossRef]
18. Basag, S.; Kocoł, K.; Piwowarska, Z.; Rutkowska, M.; Baran, R.; Chmielarz, L. Activating effect of cerium in hydrotalcite derived Cu-Mg-Al catalysts for selective ammonia oxidation and the selective reduction of NO with ammonia. *React. Kinet. Mech. Catal.* **2017**, *121*, 225–240. [CrossRef]
19. Lou, J.C.; Hung, C.M.; Yang, S.F. Selective Catalytic Oxidation of Ammonia over Copper-Cerium Composite Catalyst. *J. Air Waste Manag. Assoc.* **2004**, *54*, 68–76. [CrossRef]
20. Gang, L.; Van Grondelle, J.; Anderson, B.G.; Van Santen, R.A. Selective low temperature NH<sub>3</sub> oxidation to N<sub>2</sub> on copper-based catalysts. *J. Catal.* **1999**, *186*, 100–109. [CrossRef]
21. Jabłońska, M.; Wolkenar, B.; Beale, A.M.; Pischinger, S.; Palkovits, R. Comparison of Cu-Mg-Al-Ox and Cu/Al<sub>2</sub>O<sub>3</sub> in selective catalytic oxidation of ammonia (NH<sub>3</sub>-SCO). *Catal. Commun.* **2018**, *110*, 5–9. [CrossRef]
22. Roy, S.; Hegde, M.S.; Madras, G. Catalysis for NO<sub>x</sub> abatement. *Appl. Energy* **2009**, *86*, 2283–2297. [CrossRef]
23. Jabłońska, M.; Palomares, A.E.; Chmielarz, L. NO<sub>x</sub> storage/reduction catalysts based on Mg/Zn/Al/Fe hydrotalcite-like materials. *Chem. Eng. J.* **2013**, *231*, 273–280. [CrossRef]
24. Huang, Y.; Tong, Z.; Wu, B.; Zhang, J. Low temperature selective catalytic reduction of NO by ammonia over V<sub>2</sub>O<sub>5</sub>-CeO<sub>2</sub>/TiO<sub>2</sub>. *J. Fuel Chem. Technol.* **2008**, *36*, 616–620. [CrossRef]
25. Luong, N.T.; Okumura, H.; Yamasue, E.; Ishihara, K.N. Structure and catalytic behaviour of CuO-CeO<sub>2</sub> prepared by high-energy ball milling. *R. Soc. Open Sci.* **2019**, *6*.
26. Cavani, F.; Trifirò, F.; Vaccari, A. Hydrotalcite-type anionic clays: Preparation, properties and applications. *Catal. Today* **1991**, *11*, 173–301. [CrossRef]
27. Rives, V. Characterisation of layered double hydroxides and their decomposition products. *Mater. Chem. Phys.* **2002**, *75*, 19–25. [CrossRef]
28. Wu, J.S.; Xiao, Y.K.; Wan, J.Y.; Wen, L.R. The growth mechanism of hydrotalcite crystal. *Sci. China Technol. Sci.* **2012**, *55*, 872–878. [CrossRef]
29. Anthony, J.W.; Bideaux, R.A.; Bladh, K.W.; Nichols, M. *Handbook of Mineralogy*; Mineralogical Society of America: Chantilly, VA, USA. Available online: <http://www.handbookofmineralogy.org/search.html?p=all> (accessed on 11 December 2019).
30. Bezerra, D.M.; Rodrigues, J.E.F.; Assaf, E.A. Structural, vibrational and morphological properties of layered double hydroxides containing Ni<sup>2+</sup>, Zn<sup>2+</sup>, Al<sup>3+</sup> and Zr<sup>4+</sup> cations. *Mater. Charact.* **2017**, *125*, 29–36. [CrossRef]
31. Wegrzyn, A.; Rafalska-Łasocha, A.; Majda, D.; Dziembaj, R.; Papp, H. The influence of mixed anionic composition of Mg-Al hydrotalcites on the thermal decomposition mechanism based on in situ study. *J. Therm. Anal. Calorim.* **2010**, *99*, 443–457. [CrossRef]
32. Pérez-Ramírez, J.; Abelló, S.; Van Der Pers, N.M. Memory effect of activated Mg-Al hydrotalcite: In situ XRD studies during decomposition and gas-phase reconstruction. *Chem. A Eur. J.* **2007**, *13*, 870–878. [CrossRef]
33. Basag, S.; Kovanda, F.; Piwowarska, Z.; Kowalczyk, A.; Pamin, K.; Chmielarz, L. Hydrotalcite-derived Co-containing mixed metal oxide catalysts for methanol incineration: Role of cobalt content, Mg/Al ratio and calcination temperature. *J. Therm. Anal. Calorim.* **2017**, *129*, 1301–1311. [CrossRef]
34. Shannon, R.D. Revised effective ionic radii and systematic studies of interatomic distances in halides and chalcogenides. *Acta Cryst.* **1976**, *13*, 751–767. [CrossRef]
35. Pavel, O.D.; Zăvoianu, R.; Birjega, R.; Angelescu, E. The effect of ageing step elimination on the memory effect presented by Mg<sub>0.75</sub>Al<sub>0.25</sub> hydrotalcites (HT) and their catalytic activity for cyanoethylation reaction. *Catal. Commun.* **2011**, *12*, 845–850. [CrossRef]
36. Mascolo, G.; Mascolo, M.C. On the synthesis of layered double hydroxides (LDHs) by reconstruction method based on the “memory effect”. *Microporous Mesoporous Mater.* **2015**, *214*, 246–248.

37. Angelescu, E.; Pavel, O.D.; Birjega, R.; Florea, M.; Žvoianu, R. The impact of the “memory effect” on the catalytic activity of Mg/Al; Mg,Zn/Al; Mg/Al,Ga hydrotalcite-like compounds used as catalysts for cyclohexene epoxidation. *Appl. Catal. A Gen.* **2008**, *341*, 50–57. [[CrossRef](#)]
38. Stanimirova, T.S.; Kirov, G.; Dinolova, E. Mechanism of hydrotalcite regeneration. *J. Mater. Sci. Lett.* **2001**, *20*, 453–455. [[CrossRef](#)]
39. Guijarro, N.; Bornoz, P.; Prévot, M.; Yu, X.; Zhu, X.; Johnson, M.; Jeanbourquin, X.; Le Formal, F.; Sivula, K. Evaluating spinel ferrites  $MFe_2O_4$  ( $M = Cu, Mg, Zn$ ) as photoanodes for solar water oxidation: Prospects and limitations. *Sustain. Energy Fuels* **2018**, *2*, 103–117. [[CrossRef](#)]
40. Kong, Z.Y.; Wong, N.X.; Lum, S.W.; Tan, S.Y.; Khan, M.R.; Cheng, C.K. The application of magnesium ferrite photocatalyst for photo treatment of methylene blue. *J. Eng. Sci. Technol.* **2015**, *10*, 1–10.
41. Durrani, S.K.; Naz, S.; Mehmood, M.; Nadeem, M.; Siddique, M. Structural, impedance and Mössbauer studies of magnesium ferrite synthesized via sol–gel auto-combustion process. *J. Saudi Chem. Soc.* **2017**, *21*, 899–910. [[CrossRef](#)]
42. Taffa, D.H.; Dillert, R.; Ulpe, A.C.; Bauerfeind, K.C.L.; Bredow, T.; Bahnemann, D.W.; Wark, M. Photoelectrochemical and theoretical investigations of spinel type ferrites ( $MxFe_{3-x}O_4$ ) for water splitting: A mini-review. *J. Photonics Energy* **1997**, *2*, 5–8. [[CrossRef](#)]
43. Wanke, S.E.; Fiedorow, R.M.J. The Influence of Preparation Methods on Surface Area, Porosity and Crystallinity of Magnesium Oxide. In *Studies in Surface Science and Catalysis*; Elsevier: Amsterdam, The Netherlands, 1988; Volume 39, pp. 601–609.
44. Xu, L.; Xu, H.-Y.; Wang, F.; Zhang, F.-J.; Meng, Z.-D.; Zhao, W.; Oh, W.-C. Microwave-Assisted Synthesis of Flower-like and Plate-like CuO Nanopowder and Their Photocatalytic Activity for Polluted Lake Water. *J. Korean Ceram. Soc.* **2012**, *49*, 151–154. [[CrossRef](#)]
45. Camtakan, Z.; Erenturk, S.; Yusan, S. Magnesium oxide nanoparticles: Preparation, characterisation, and uranium sorption properties. *Environ. Prog. Sustain. Energy* **2011**, *31*, 482–489. [[CrossRef](#)]
46. Radhakrishnan, A.A.; Beena, B.B. Structural and optical absorption analysis of CuO nanoparticles. *Indian J. Adv. Chem. Sci.* **2014**, *2*, 28–35.
47. Altincekic, T.G.; Boz, I.; Baykal, A.; Kazan, S.; Topkaya, R.; Toprak, M.S. Synthesis and characterization of  $CuFe_2O_4$  nanorods synthesized by polyol route. *J. Alloys Compd.* **2010**, *493*, 493–498. [[CrossRef](#)]
48. Sagar, G.V.; Rao, P.V.R.; Srikanth, C.S.; Chary, K.V.R. Dispersion and reactivity of copper catalysts supported on  $Al_2O_3$ - $ZrO_2$ . *J. Phys. Chem. B* **2006**, *110*, 13881–13888. [[CrossRef](#)] [[PubMed](#)]
49. Shi, X.; Chu, B.; Wang, F.; Wei, X.; Teng, L.; Fan, M.; Li, B.; Dong, L.; Dong, L. Mn-Modified CuO,  $CuFe_2O_4$ , and  $\gamma$ - $Fe_2O_3$  three-phase strong synergistic coexistence catalyst system for NO reduction by CO with a wider active window. *ACS Appl. Mater. Interfaces* **2018**, *10*, 40509–40522. [[CrossRef](#)] [[PubMed](#)]
50. Wang, Y.; Xue, R.; Zhao, C.; Liu, F.; Liu, C.; Han, F. Effects of Ce in the catalytic combustion of toluene on  $Cu_xCe_{1-x}Fe_2O_4$ . *Colloids Surfaces A Physicochem. Eng. Asp.* **2018**, *540*, 90–97. [[CrossRef](#)]
51. Do, J.Y.; Son, N.; Park, N.K.; Kwak, B.S.; Baek, J.I.; Ryu, H.J.; Kang, M. Reliable oxygen transfer in  $MgAl_2O_4$  spinel through the reversible formation of oxygen vacancies by  $Cu^{2+}/Fe^{3+}$  anchoring. *Appl. Energy* **2018**, *219*, 138–150. [[CrossRef](#)]
52. Pang, S.C.; Chin, S.F.; Anderson, M.A. Redox equilibria of iron oxides in aqueous-based magnetite dispersions: Effect of pH and redox potential. *J. Colloid Interface Sci.* **2007**, *311*, 94–101. [[CrossRef](#)]
53. Bodade, A.B.; Taiwade, M.A.; Chaudhari, G.N. Bioelectrode based chitosan-nano copper oxide for application to lipase biosensor. *J. Appl. Pharm. Res.* **2017**, *5*, 30–39.
54. Noerochim, L.; Indra, M.A.T.; Purwaningsih, H.; Subhan, A. Porous  $Fe_2O_3$  Microspheres as Anode for Lithium-Ion Batteries. *IOP Conf. Ser. Mater. Sci. Eng.* **2018**, *367*, 012038. [[CrossRef](#)]
55. Shang, H.; Zhang, X.; Xu, J.; Han, Y. Effects of preparation methods on the activity of CuO/CeO<sub>2</sub> catalysts for CO oxidation. *Front. Chem. Sci. Eng.* **2017**, *11*, 603–612. [[CrossRef](#)]
56. Tang, X.; Zhang, B.; Li, Y.; Xu, Y.; Xin, Q.; Shen, W. CuO/CeO<sub>2</sub> catalysts: Redox features and catalytic behaviors. *Appl. Catal. A Gen.* **2005**, *288*, 116–125. [[CrossRef](#)]
57. Jabłońska, M.; Chmielarz, L.; Wegrzyn, A.; Guzik, K.; Piwowska, Z.; Witkowski, S.; Walton, R.I.; Dunne, P.W.; Kovanda, F. Thermal transformations of Cu-Mg (Zn)-Al(Fe) hydrotalcite-like materials into metal oxide systems and their catalytic activity in selective oxidation of ammonia to dinitrogen. *J. Therm. Anal. Calorim.* **2013**, *114*, 731–747. [[CrossRef](#)]

58. Yue, W.; Zhang, R.; Liu, N.; Chen, B. Selective catalytic oxidation of ammonia to nitrogen over orderly mesoporous CuFe<sub>2</sub>O<sub>4</sub> with high specific surface area. *Chinese Sci. Bull.* **2014**, *59*, 3980–3986. [[CrossRef](#)]
59. Zhang, L.; Liu, F.; Yu, Y.; Liu, Y.; Zhang, C.; He, H. Effects of adding CeO<sub>2</sub> to Ag/Al<sub>2</sub>O<sub>3</sub> catalyst for ammonia oxidation at low temperatures. *Cuihua Xuebao/Chinese J. Catal.* **2011**, *32*, 727–735. [[CrossRef](#)]
60. Jabłońska, M. Selective catalytic oxidation of ammonia into nitrogen and water vapour over transition metals modified Al<sub>2</sub>O<sub>3</sub>, TiO<sub>2</sub> and ZrO<sub>2</sub>. *Chem. Pap.* **2015**, *69*, 1141–1155. [[CrossRef](#)]
61. Gang, L.; Anderson, B.G.; Van Grondelle, J.; Van Santen, R.A. NH<sub>3</sub> oxidation to nitrogen and water at low temperatures using supported transition metal catalysts. *Catal. Today* **2000**, *61*, 179–185. [[CrossRef](#)]



© 2020 by the authors. Licensee MDPI, Basel, Switzerland. This article is an open access article distributed under the terms and conditions of the Creative Commons Attribution (CC BY) license (<http://creativecommons.org/licenses/by/4.0/>).